DOKUZ EYLÜL UNIVERSITY
GRADUATE SCHOOL OF NATURAL AND APPLIED SCIENCES

THERMAL DESIGN AND OPTIMIZATION OF SHELL AND TUBE HEAT EXCHANGERS USED IN ORGANIC RANKINE CYCLES

by
Anıl ERDOĞAN

July, 2017
İZMİR

THERMAL DESIGN AND OPTIMIZATION OF SHELL AND TUBE HEAT EXCHANGERS USED IN ORGANIC RANKINE CYCLES

A Thesis Submitted to the
Graduate School of Natural and Applied Sciences of Dokuz Eylül University
In Partial Fulfillment of the Requirements for the Master of Science of
Department of Mechanical Engineering

by
Anıl ERDOĞAN

July, 2017
İZMİR

M.Sc THESIS EXAMINATION RESULT FORM

We have read the thesis entitled **"THERMAL DESIGN AND OPTIMIZATION OF SHELL AND TUBE HEAT EXCHANGERS USED IN ORGANIC RANKINE CYCLES"** completed by **ANIL ERDOĞAN** under supervision of **ASSOC. PROF. DR. CAN ÖZGÜR ÇOLPAN** and we certify that in our opinion it is fully adequate, in scope and in quality, as a thesis for the degree of Master of Science.

Assoc. Prof. Dr. Can Özgür Çolpan

Supervisor

Prof. Dr. Serhan Küçüka

(Jury Member)

Prof. Dr. T. Hikmet Karakoç

(Jury Member)

Prof.Dr. Emine İlknur CÖCEN
Director
Graduate School of Natural and Applied Sciences

ACKNOWLEDGMENT

The author wishes to express deep gratitude to his supervisor Assoc. Prof. Dr. Can Özgür ÇOLPAN for their invaluable supervision, advice, encouragement, support, and insight throughout the research process.

The author also thanks to all faculty members of the Mechanical Engineering Department for their instructions during his graduate studies.

The author also thanks to Prof. Dr. Serhan KÜÇÜKA and Prof. Dr. T. Hikmet KARAKOÇ for their contributions with their comments in this study.

The author would like to express sincere thanks to Dr. David Ouellette, a postdoctoral researcher from University of Toronto, for his support.

The author wishes to express his special thanks to his dear friend Mrs. Duygu Melek Çakıcı for her valuable contributions in this study.

The author wishes to express his special thanks to his dear friend Ms. Yağmur Nalbant for her contribution and support in this thesis.

The author would also like to thank to his dear friends Oğuz Kemer and Arda Berk Tanrısever for his support in this thesis.

The author gratefully thanks to his parents Tahsin and Şenay Erdoğan, his brother Mertcan Erdoğan, and his aunt Gülay Hakvar for their invaluable support in his entire life.

Anıl ERDOĞAN

THERMAL DESIGN AND OPTIMIZATION OF SHELL AND TUBE HEAT EXCHANGERS USED IN ORGANIC RANKINE CYCLES

ABSTRACT

In this thesis, the design and analysis of a shell and tube heat exchanger used to combine parabolic trough solar collectors and an organic Rankine cycle based geothermal power plant is presented. A thermal model for the parabolic trough solar collector was first used to find the temperature of the thermal oil entering the heat exchanger under different solar irradiation intensity. Then, a detailed thermal model for the shell and tube heat exchanger based on logarithmic mean temperature difference method was formed. In addition, for this heat exchanger, the temperature and velocity variations were examined in a solar - geothermal shell and tube heat exchanger in a COMSOL Multiphysics® environment. On the other hand, a detailed thermal model for a shell and tube heat exchanger used in an organic Rankine cycle was formed. Two different configurations of the cycle was considered, which are subcritical and supercritical organic Rankine cycles. For this purpose, the heat exchanger was divided into several zones and the outlet conditions of each zone were calculated applying logarithmic mean temperature difference method. Different Nusselt correlations according to the relevant phase (single, two-phase and supercritical) were also used in this model. A parametric study was conducted to assess the effect of some key design parameters (e.g. diameter of the tubes, tube length, baffle spacing, the type of working fluid, solar irradiation, and source temperature) on the performance of the heat exchanger. The performance parameters are taken as the heat transfer surface area, pumping power, overall heat transfer coefficient, and total pressure drop. As a result of these parametric studies, the design and operating parameters and the working fluid that give the best performance for the heat exchanger are found.

Keywords: Shell and tube heat exchanger, log mean temperature difference method, Engineering Equation Solver, COMSOL Multiphysics®, organic Rankine cycle, modeling

ORGANİK RANKINE ÇEVRİMLERİNDE KULLANILAN GÖVDE BORU TİPİ ISI DEĞİŞTİRİCİSİNİN ISIL TASARIMI VE OPTİMİZASYONU

ÖZ

Bu tez çalışmasında parabolik oluklu güneş kolektörü ile jeotermal temelli organik Rankin çevriminde hibrit olarak yer alan gövde boru tipi ısı değiştiricisinin tasarım ve analizi sunulmuştur. Parabolik oluklu güneş kolektörü için termal model kullanılarak kolektör akışkanının ısı değiştiricisine giriş sıcaklığı farklı güneş radyasyonu şiddetleri altında bulunmuştur. Daha sonra gövde boru tipi ısı değiştiricisi için logaritmik ortalama sıcaklık farkı metodu kullanılarak detaylı bir ısıl model oluşturulmuştur. Buna ek olarak bahsedilen bu ısı değiştiricisi için COMSOL Multiphysics® programında sıcaklık ve hız dağılımları sayısal yöntemlerle bulunmuştur. Öte yandan jeotermal kaynak ile organik Rankin çevriminde hibrit olarak yer alan gövde boru tipi ısı değiştiricisi için de detaylı bir ısıl model oluşturulmuştur. Süper kritik ve kritik altı olmak üzere iki farklı çevrim konfigürasyonunda bu modelleme yapılmıştır. Bu amaçla, ısı değiştiricisi birden fazla bölgeye ayrılarak her bir bölge için çıkış şartları logaritmik ortalama sıcaklık farkı metoduyla bulunmuştur. Bu model de farklı Nusselt bağıntıları belli fazlar (tek faz, iki fazlı ve süper kritik) için kullanılmıştır. Parametrik çalışma yapılarak bazı önemli parametrelerin (boru çapı, boru uzunluğu, şaşırtma levhası mesafesi, çevrim akışkanı çeşidi, güneş radyasyonu şiddeti ve kaynak sıcaklığı) ısı değiştiricisi performansına etkisi değerlendirilmiştir. Bu performans parametreleri ısı transferi yüzey alanı, pompa gücü, toplam ısı geçiş katsayısı, toplam basınç düşümü şeklindedir. Bu parametrik çalışmalar sonucunda, ısı değiştiricisi için en iyi performansı veren tasarım, çalışma parametreleri ve çalışma sıvısı bulunur.

Anahtar kelimeler: Gövde boru tipi ısı değiştiricisi, logaritmik ortalama sıcaklık metodu, Engineering Equation Solver, COMSOL Multiphysics, organik Rankin çevrimi, modelleme

CONTENTS

Page

LIST OF FIGURES

Page

LIST OF TABLES

Page

CHAPTER ONE
INTRODUCTION

1.1 Introduction

Fossil fuels like coal and natural gas have been used as main energy resources since the beginning of the industrial revolution. Traditionally, fossil fuels have been converted into electricity using different technologies such as internal combustion engine, steam turbine, and gas turbine. Nowadays fossil fuels have started to be replaced with renewable energy resources such as wind, geothermal, solar, ocean, and hydro in the stationary power production as the depletion of fossil fuels and the concerns on the environmental issues (e.g. depletion of ozone layer, air pollution, acid rains, and global warming) have increased. For these reasons, researchers have preferred using renewable energy resources and they have developed technologies based on these resources to generate electricity.

Turkey is one of the richest countries in terms of renewable resources in the world. In the recent years, various incentives have been made by governments and also non-governmental organizations on the use of renewable energy in Turkey. It is also aimed to raise public awareness by emphasizing the importance of renewable energy by government. Turkey is in a geopolitically important location in the world as it is surrounded by three seas and has high potential of renewable resources. In terms of geothermal energy, Turkey is ranked the first in Europe; seventh in the world. For wind energy, in last ten years, the capacity of wind energy dramatically increases from 20 MW to 4500 MW. On the other hand, the hydroelectric power capacity can now be reached to 236 MW. As a result of the new energy technologies and Turkey's renewable energy location, the importance of the energy resources has been understood by government and civil society organizations; and there has been more interest in renewable energy resources and development of its technologies with the support of the government programs.

1.2 Motivation

As discussed in Section 1.1, several factors such as the global energy supply security and the need for generating efficient and clean energy have increased the interest in research related to renewable energy technologies. In this regard, geothermal power plants have been built where the geothermal sources are available, and these plants have been widely used for generating electricity in the recent years. In last decades, geothermal energy systems have been combined with other kind of technologies based on renewable resources (e.g. solar) to increase the electricity generation and thermal efficiency, where applicable.

Organic Rankine cycle is a very promising technology for converting low-grade energy resources such as geothermal energy, solar energy, and recovered waste heat to utilize electrical energy. Although ORC technology is not new, researchers still work on the development of this cycle to increase the cycle efficiency and electricity generation. In order to have high performance of these cycles, suitable design and selection of the cycle components should be done. Heat exchangers have a vital part in the ORC system because it affects the cycle efficiency and cost significantly. In most studies found in the literature, the heat exchanger is taken as a black box thus the performance of the entire system is found performing energy and exergy analyses. However, it is very important to make a detailed design for the heat exchangers on the geothermal power systems. Based on this prediction, a detailed thermal model for heat exchanger integrating parabolic trough solar collector and organic Rankine cycle was developed and performance analyses were carried out in this thesis. On the other hand, the thermal model for the heat exchanger integrating organic Rankine cycle and geothermal source was performed. This model differs from the other models found in the literature in that the heat exchanger is divided into several zones to distinguish single-zone, two-phase-zone and supercritical-zone. This model also provides a better understanding of the performance of the heat exchanger as well as the entire system.

1.3 Objective

The aim of this thesis is to design and analyze a shell and tube heat exchanger that combines PTSC and ORC, and ORC and geothermal sources. For this purpose, thermal models for the PTSC and heat exchanger were first developed. Then, a parametric study was conducted to study the effect of important design parameters (e.g. outer diameter, tube length, baffle spacing, number of pass, and organic Rankine cycle working fluid types) on the output parameters (e.g. the heat transfer surface area and the pumping power). In addition, the effect of solar irradiation intensity on the heat exchanger performance was assessed. On the other hand, a detailed thermal model for a shell and tube heat exchanger used in different ORC cycle configurations, which are subcritical and supercritical ORC, was developed and the equations originating from this model were solved using EES. For this purpose, the shell and tube heat exchanger was divided into several zones. Different Nusselt correlations for the single phase, two phase, and supercritical conditions were used. In addition, a parametric study was conducted to investigate the effect of some key design and operating parameters (inner diameter of the tubes and inlet temperature of the turbine) on the performance of the shell and tube heat exchangers. The performance parameters are the overall heat transfer coefficient, the tube side pressure drop according to dividing zones in the heat exchangers. In addition the effect of ORC source temperature on the performance of the heat exchanger according to different design methods which are single zone and multi zone is investigated.

1.4 Thesis Outline

The following chapter provides an overview of renewable energy resources and technologies, heat exchangers and its types, organic Rankine cycles and its architectures, and hybridization of solar geothermal technologies. A literature review on the heat exchanger modeling, modeling of organic Rankine cycle, and hybrid solar – geothermal and other hybrid technologies are also included.

The third chapter includes system description, modeling techniques and several analytical and numerical equations for heat exchangers and parabolic trough solar collectors. Firstly, general information about the system and its equipment (e.g. the parabolic trough solar collectors, and the heat exchangers) are outlined. Secondly, the analytical and CFD modeling techniques and its equations are explained. Finally, the modeling techniques and the equations of parabolic trough solar collectors are discussed.

The fourth chapter includes the results and discussion of the heat exchangers integrating organic Rankine cycle and parabolic trough solar collectors, and organic Rankine cycle and geothermal source that were carried out using the models discussed in Chapter 3. The several parametric studies are also included in this chapter.

In the last chapter, the conclusions derived from this thesis are discussed.

CHAPTER TWO
RENEWABLE ENERGY SOURCES AND TECHNOLOGIES

2.1 Introduction

This chapter gives general and brief information about renewable energy technologies which are solar, wind, geothermal, hydropower, and biomass, and bioenergy, heat exchangers and its types, organic Rankine cycle, and hybridization of solar geothermal technologies. First of all, an introduction to renewable energy resources and technology is made. Secondly, the heat exchanger and its types, and organic Rankine cycle technology are presented. Finally, recent studies in the literature on the heat exchanger modeling, geothermal power plant based on organic Rankine cycle, and hybridization of solar geothermal systems are discussed.

2.2 Renewable Energy

Renewable energy is a type of energy that is gained from renewable resources such as solar, wind, rain, tides, ocean, and geothermal. In recent years, researchers have shifted to conducting research on renewable energy resources due to the harmful effects of fossil fuels on the environment. Renewable energy can be mainly utilized in four important areas: electricity production, heating, cooling, and transportation.

According to REN21's (the Renewable Energy Policy Network for 21st Century) 2016 report, renewables conduced 19.2% to global energy consumption (2014 data) and 23.7% to the generation of electricity (2015 data) (Zervos, 2016). This energy consumption is divided into different kind of renewables such as 8.9% coming from biomass, 4.2% from modern biomass, geothermal and solar heat, 3.9% from hydro energy, and 2.2% from electricity generation from solar, wind, and geothermal ("Union of Concerned Scientists", 2017). Investments in renewable energy still increase in the world. More than 286 billion $ in 2015 with countries like China and the United States invested in wind, solar, biofuels, and hydro (Zervos, 2016). In the world, there are approximately 8 million jobs associated with renewable energy

industries with photovoltaics being the largest renewable employer (Zervos, 2016). In 2015, more than half of all renewable based electricity plants were installed. In addition, Table 2.1 shows the renewable energy indicators for investment, power, heat, transport, and policies according to 2014 and 2015 data. It can be clearly interpreted from this table that the interest in renewable energy and its technologies has increased.

Table 2.1 Renewable energy indicators (Zervos, 2016)

		2014	**2015**
INVESTMENT			
New investment in renewable power and fuel	billion USD	273	285.9
POWER			
Renewable power capacity (not included hydro)	GW	665	785
Renewable power capacity (included hydro)	GW	1701	1849
Hydropower capacity	GW	1036	1064
Bio-power capacity	GW	101	106
Bio-power generation (annual)	TW·h	429	464
Geothermal power capacity	GW	12.9	13.2
Solar PV capacity	GW	177	227
Concentrating solar thermal power capacity	GW	4.3	4.8
Wind power capacity	GW	370	433
HEAT			
Solar hot water capacity	GW	409	435
TRANSPORT			
Ethanol production (annual)	billion liters	94.5	98.3
Biodiesel production (annual)	billion liters	30.4	30.1
POLICIES			
Countries with policy targets		164	173

Table 2.1 Renewable energy indicators (Zervos, 2016) (continue)

States/provinces/countries with feed-in policies		110	110
States/provinces/countries with RPS/quota policies		98	100
Countries with tendering / public competitive bidding		60	64
Countries with heat obligation/mandate		21	21
Countries with biofuel mandates		64	66

Renewable energy technologies can be classified according to the types of electricity conversion technologies. Each technology has its own benefits and challenges. A brief information on renewable energy resources including solar energy, wind energy, geothermal energy, hydro energy, and biomass energy is given in the following paragraphs.

Solar energy, radiant light and heat from the sun, which is located in the center of the solar system, can be utilized using different technologies such as concentrated solar power (CSP) technologies, photovoltaics, concentrated photovoltaics, and artificial photosynthesis (Duffie and Beckman, 2013; Zervos, 2016). The sun's energy is approximately 1300 W/m^2 in the out of the atmosphere. However when it reaches the atmosphere, approximately one-third of solar light is reflected back into the space. Nowadays, because of its zero emission during its operation, the sun energy is used for generating electricity with photovoltaic panels (PV) and concentrating solar power (CSP). An example for the usage of the solar collector for electricity generation is given in Figure 2.1.

Figure 2.1 Solar towers in Spain for electricity generation (Institute for Energy Resourcefulness, 2017)

Wind energy can be described basically as follows. Air streams can be utilized to run wind turbines and generate electricity. Generating electricity from wind energy includes no toxic emissions and no trapping heat that contributes global warming. The usage of wind energys is growing yearly as the source of electricity generation in the world. For example, based on the open literature, 45000 MW of new capacity using wind energy were installed in worldwide in 2011 (GWEC, 2012; National Renewable Energy Laboratory, 2010). A photograph of wind turbines is given in Figure 2.2.

Figure 2.2 Wind turbines (Union of Concerned Scientists, 2017)

Geothermal energy is defined as heat coming from the earth core where the stemperature is at approximately 5500°C (DiPippo, 2012). Geothermal is used as an energy source for a long time. In ancient time, geothermal energy is used for bathing, washing, and cooking. The Romans and the Japanese used thermal springs for health since eight century. In the middle ages Arabian and Turkish people developed traditional thermal baths (Hepbasli and Ozgener, 2004). These uses pioneer the modern balneological industry. Geothermal energy is used in various fields in healthcare. These are bathing, wellness, spa, district heating, heating, and cooling, food

drying, canned food industry, drying cement, and power generation. As an example, a photograph of view of an existing power plant, namely Kızıldere geothermal power plant, is given in Figure 2.3.

Figure 2.3 Kızıldere geothermal power plant (Enerji Enstitüsü, 2011)

Water is one of the mostly used renewable resources for generating electricity. Hydropower is supplied from falling water or very fast flowing water. Hydroelectricity energy is supplied from hydropower. Hydropower is produced and widely used in nearly 150 countries. 33% of global hydropower is provided by Asia-Pacific region. For this purpose, China is the largest hydroelectricity producer (Zervos, 2016). There are several advantages of hydropower such as low cost, high value power, and suitability for industrial applications. In addition, CO_2 emissions reduce with the usage of this technology. In addition to the advantages of hydropower, there are disadvantages of using hydropower as follows: ecosystem damage, loss of lands, siltation, and flow shortage. The general view of Balbina Hydroelectric plant is presented in Figure 2.4.

Figure 2.4 Balbina hydroelectric plant, Brazil

Biomass is produced from living or recently living organisms. As an energy resource, biomass can either be used directly with combustion to produce heat and electricity, or can be indirectly converted into various forms of biofuel through some chemical processes. The conversation of biomass to biofuel can be achieved by various methods such as thermal, chemical, and biochemical reactions (Biomass, 2016). Examples to industrial biomass can be given as miscanthus, hemp, corn, bamboo, eucalyptus, and palm oil. The eucalyptus tree in Brazil, which can be used to generating electricity, is presented in Figure 2.5.

Figure 2.5 The eucalyptus tree in Brazil for electricity generation (Biomass, 2016)

2.3 Heat Exchangers

Heat exchanger is a device that the heat transfer between one or two fluids. This fluids could be separated by a solid wall to avoid mixing or may be direct contact. The heat exchangers are widely used in many applications such as space heating, central heating, geothermal power plants, food processing, oil refineries, air conditioning, and refrigeration. The heat exchangers can be classified according to construction type. These are shell and tube heat exchangers, plate heat exchangers, fin and tube heat exchangers, and compact heat exchangers. The general information about the types of heat exchanger is given in the following subsections.

2.3.1 Shell and Tube Heat Exchangers

The shell and tube heat exchanger is a type of heat exchanger. This type of heat exchangers consist of a tube with circular cross section called as shell, several tubes

are mounted into shell, and baffles which are used for flow regulation in the shell side fluid. The shell and tube heat exchangers are widely used range of between 35% - 40% in practice (Zhang, He, & Tao, 2009). Among the different types of heat exchangers, the shell and tube heat exchangers are preferred for space heating, power production, and chemical processing applications. The main advantages of this heat exchanger type over other types can be listed as follows. There is substantial flexibility regarding their materials to accommodate corrosion and other concerns; they can be used in systems with higher operating temperatures and pressures; and tube leaks are easily located and plugged since pressure test is comparatively easy (Perry, Green, & Maloney, 1997; Subramanian, 2010a, 2010b). However, this heat exchanger requires more space; and cleaning and maintenance are difficult since a tube requires sufficient amount of clearance at one end to remove the tube nest. Shell and tube heat exchangers are classified and built according to the widely used Tubular Exchange Manufactured Association (TEMA) standards (Harrison, 2007). This type of heat exchangers can be categorized according to the number of tube passes. The simplest form is one tube pass as shown in Figure 2.6. Two tube passes and three tube passes configurations are shown in Figure 2.7 and Figure 2.8, respectively. Baffles are often installed to increase heat transfer coefficient of the shell side fluid. In addition, they are fixed to the tubes to reduce tube vibration.

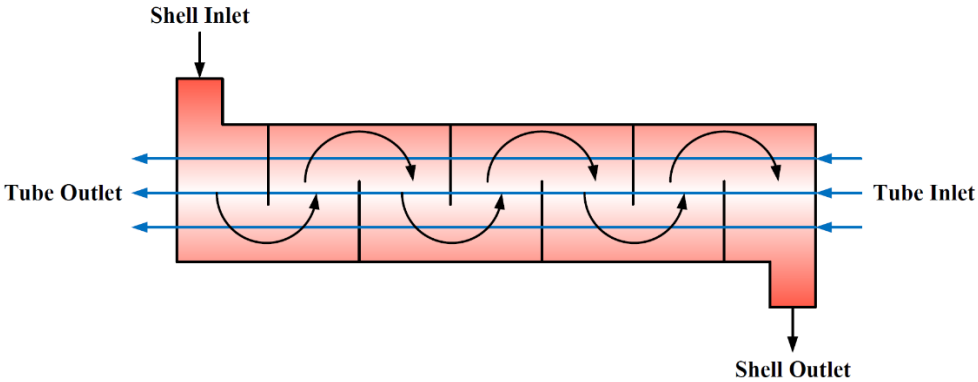

Figure 2.6 One tube pass shell and tube heat exchanger

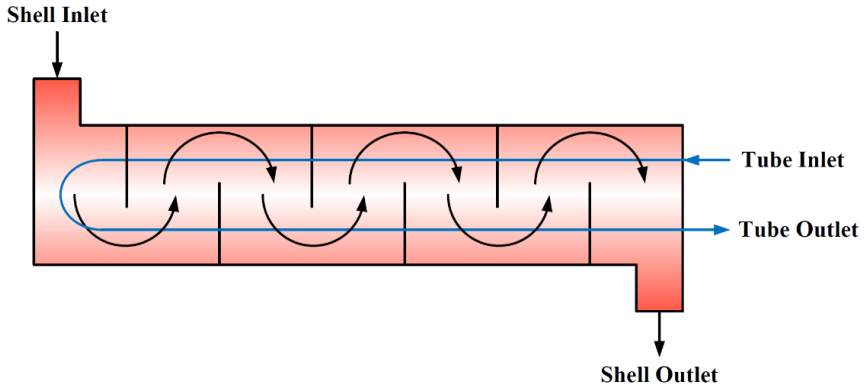

Figure 2.7 Two tube passes shell and tube heat exchangers

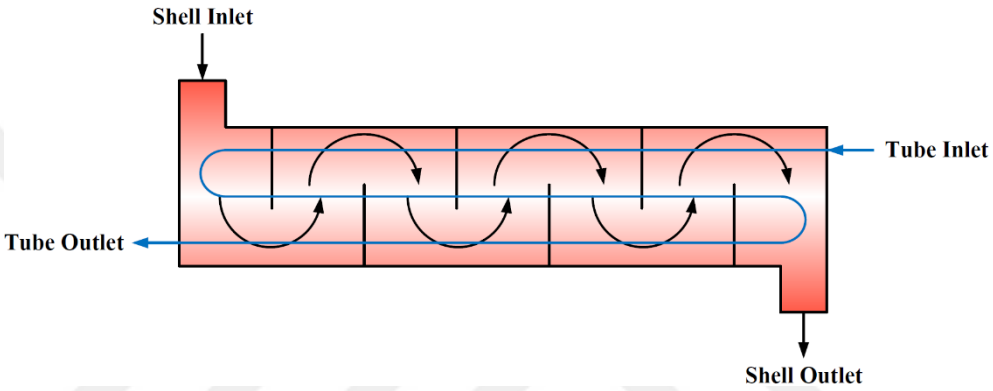

Figure 2.8 Three tube passes shell and tube heat exchangers

2.3.2 Plate Heat Exchangers

Plate heat exchanger is another type of heat exchanger that consists of many thin slightly separated plates which provide large surface areas and small fluid flow passages for heat transfer. Thanks to the advances in gasket and brazing technology, the application of plate type heat exchanger has increased. These type of heat exchangers are gasket type which provide easiness in assembly, disassembly, cleaning, and checking leaks. When the plate type heat exchangers are compared with other type of heat exchangers, they have lower volume and cost; and they operate at low to medium operating pressures. Other feature of this heat exchanger is that they provide counter flow. This allows high temperature changes, thus the heat transfer efficiency increases. A schematic of the plate type heat exchanger is given in Figure 2.9.

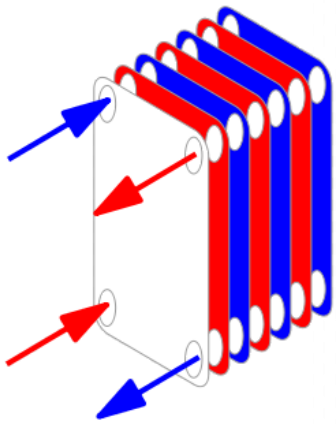

Figure 2.9 The plate type heat exchanger (Heat Exchangers, n.d.)

2.3.3 Finned Tube Heat Exchanger

Another type of heat exchanger is finned tube heat exchanger. This heat exchanger provides the heat transfer between gases and liquids, significantly saves space and thus it is more efficient than straight tube heat exchangers. The finned tube heat exchanger is used in many applications, such as power plants with as an exhaust gas heat exchanger, industrial dryers, and air conditions. An example to finned tube heat exchanger is given in Figure 2.10.

Figure 2.10 The finned tube heat exchanger (Indiamart, 2017)

2.3.4 Compact Heat Exchanger

Compact heat exchanger is another type of heat exchanger. They allow a higher heat transfer rate and requires less volume and less weight as compared to other heat exchanger types. In order to increase the heat transfer and its surface area, the fin constructions are used in compact heat exchangers. They are the preferred choice for applications which require higher heat transfer rate in a limited volume such as air conditioning and automotive radiators. A representative compact heat exchanger is presented in Figure 2.11.

Figure 2.11 Compact heat exchanger (Heat Exchangers, n.d.)

2.4 Organic Rankine Cycles

The organic Rankine cycle (ORC) uses organic carbon-based fluids that change phase from liquid to vapor at lower temperatures and pressures than the phase change of water to steam. The organic fluid allows heat recovery from low temperature heat sources such as waste heat recovery, biomass, solar, geothermal, and diesel engine exhaust. These heat sources are converted into electricity in this cycle.

The working principle of ORC is similar to the traditional Rankine cycle; however its main difference from the traditional cycle is the type of fluid used. The working principle of ORC is given basically as follows. The working fluid first enters the boiler, the evaporator, where it is evaporated to change the phase from liquid to vapor, then it passes through the expander, and then passes the condenser, where the heat is rejected,

to complete the cycle. In the ideal ORC, which has no irreversibilities, the expansion process is isentropic, and the condensation and the evaporation processes are isobaric; whereas in real cycle, the irreversibilities cause decrease in the cycle efficiency.

In order to increase the cycle efficiency, the cycle can be improved by using regenerator. Thanks to the regenerator, in general, the organic fluid does not reach the two phase state at the turbine outlet. At this point, the temperature of working fluid is higher than the condensation temperature. This higher temperature fluid can be used to preheat the liquid entering the evaporator. Another improvement could be the usage of supercritical cycle. In this cycle, temperature of working fluid entering the expander reaches higher temperature than critical temperature of the working fluid. At this cycle configuration, more power could be produced than the subcritical ORC.

The fluid selection is one of the most important factors affecting the performance of an integrated solar-geothermal system. Generally, a suitable working fluid should have the following properties in order to have favorable thermodynamic characteristics and low environmental impact in this system: high specific heat, high thermal conductivity, low viscosity, non-corrosive, non-toxic, and low ODP and GWP values (Cakici, Erdogan, & Colpan, 2016; Mago, Chamra, & Somayaji, 2007; Qiu, 2012; Wang et al., 2011). The mostly used ORC working fluid which is found from the literature is given in Table 2.2.

Table 2.2 The properties of the selected ORC side fluids (*ASHRAE*, 2008, Linde Gas, 2015).

ORC Side Working Fluids	**GWP[a]**	**ODP[b]**	**ASHRAE 34 Safety Group**	**ASHRAE Flammability**	**ASHRAE Toxicity**
Ammonia	0	0	B2L	Yes	Yes
R22	1810	0.055	A1	No	No
R134a	1430	0	A1	No	No
R404a	3922	0	A1	No	No
R407c	1774	0	A1	No	No
R423a	2280	0	A1	No	No
R502	4657	0.23	A1	Yes	No
R507a	3985	0	A1	No	No
R600	4	0	A1	No	No
R41	97	0	A2	No	No
R218	8830	0	A1	No	No
R143a	3800	0	A2	No	No
R125	3400	0	-	-	-
R245fa	1030	0	A1	No	No
R1234yf	4	0	A2L	Yes	No
R236ea	1200	0	-	-	-
R152a	124	0	A2	Yes	No
R124	610	0.03	A1	No	No
R142b	2400	0.043	A2	No	No
R290	3	0	A3	Yes	No
Isobutane	3	0	A3	Yes	No

2.5 Hybridization of Solar – Geothermal Technologies

Hybrid power plant uses different energy sources for producing electricity. In hybrid system, two or more sources such as solar, wind, geothermal, biomass and hydro can be combined in order to increase the net power output and overall system efficiency.

There are some hybrid applications in the world. For example, a wind is hybridized with wind power system on Ramea, in Canada (Wind Hybrid Power

Systems, 2016). Yazd plant where hybridized with solar and geothermal sources (US' DOE Announces $20 M to Integrate Concentrated Solar Power with Fossil Fuel Plants, 2012). In Florida The Martin Next Generation Solar Center where adds 75 MW of concentrated solar power to the gas plant. Ain Beni Matar in Morocco, Kuraynat in Egypt, and Hassi R'mell in Algeria (Hybrid Plant, 2015).

2.6 Literature Survey

2.6.1 Heat Exchanger Modelling

Numerous studies are available in the literature on the modelling of heat exchangers. These studies can be categorized according to the analytical modelling of shell and tube heat exchangers and CFD modelling of shell and tube heat exchangers.

There are some studies on the design, modeling, and optimization of the shell and tube heat exchangers using analytical approaches in the literature. For example, Kara & Güraras (2004) created 240 alternative exchanger configurations and the computer program that they developed selects the optimum configuration among the all possible exchanger configurations. The shell diameter, baffle spacing, number of pass are the parameters that can be changed in this program. The program then determines the overall dimensions of the shell and the optimum heat transfer surface area required to meet the specified heat transfer duty by calculating minimum or allowable shell-side pressure drop. The results of their study showed that triangular tube pitch layout with one or two tube pass yields the best performance. Reppich & Zagermann (1995) developed a computer based design model to determine the optimum dimensions of segmentally baffled shell and tube heat exchangers by calculating optimum shell side and tube side pressure drops using the equations provided in their work. The optimized design parameters were selected as number of tubes, tube length, shell diameter, number of baffles, baffle spacing, and baffle cut. The proposed model also includes a cost analysis. Selbaş, Kızılkan, & Reppich (2006) created a mathematical model of the heat exchanger, which was coded and solved in MATLAB environment. Dittus-Boelter equation and Bell and Delaware method were used to calculate the tube and

shell side heat transfer coefficients, respectively. Logarithmic Mean Temperature Difference (LMTD) method was used to analyze the heat exchanger. They also performed a cost analysis to study the effect of six different variables (outer tube diameter, tube layout, number of tube passes, shell diameter, baffle spacing, and baffle cut) on the heat transfer surface area and shell side fluid velocity. In the paper by Walraven, Laenen, & D'haeseleer (2014), the system optimization of different configurations of ORCs having either plate heat exchangers or shell and tube heat exchangers were compared. They also created a mathematical model for integrated ORC systems; and compared the performance of the systems when different fluids are used. Their study showed that ORCs with all plate heat exchangers perform mostly better than ORCs with all shell and tube heat exchangers. Different tube configurations were investigated in the paper by Walraven, Laenen, & D'haeseleer (2014). Their study concluded that the 30° and 60° tube configurations should be used for the single phase and two phase heat exchangers, respectively. Fettaka, Thibault, & Gupta (2013) developed a mathematical model for the shell and tube heat exchangers, and nine different optimization studies were carried out by using different geometric parameters (tube layout, number of the tube passes, baffle spacing, baffle cut, tube to baffle diametrical clearance, tube length, tube outside diameter, tube wall thickness, and shell to baffle diameter clearance). Erdogan, Colpan, & Cakici (2017) developed a thermal model for a shell and tube heat exchanger used to combine parabolic trough solar collectors (PTSCs) and an organic Rankine cycle (ORC) based geothermal power plant. A computer code was written using Engineering Equation Solver (EES) to study the effect of some key design parameters on the heat transfer surface area of the heat exchanger and the pumping power. Furthermore an optimization study using two stage Taguchi method is performed to find the design parameters that minimize the heat transfer surface area and pumping power. The results show that, the baffle spacing is the most dominant design parameter; Therminol VP1 or Dowtherm A as the PTSC side fluid and R245fa or R600 as the ORC side fluid should be selected for maximizing the performance of the system.

There are some studies on the design, modeling, and optimization of the shell and tube heat exchangers using CFD approaches in the literature. You et al. (2015)

conducted a numerical study on shell and tube heat exchanger with the tre-foil baffles. They made a structural modification which cancelled the last piece of baffle and improve the thermo-hydraulic performance. Also they investigated the effect of baffle distance. They found that with the structural modification the flow resistance on shell side is decreased by 21%. The overall thermo-hydraulic performance on the shell side is increased by 21.9%. Ozden & Tari (2010) developed a numerical model for shell side of a small shell and tube heat exchanger. They obtained shell side heat transfer coefficient, pressure drop, and the heat transfer rate from CFD simulation results. The results of this study shows that Bell and Delaware method, k-ε realizable turbulence model with first order discretization is selected as the best simulation approach. Wang et al. (2017) proposed a double shell side rod baffle heat exchanger, and compared with single rod baffle heat exchanger as well as numerically. They changed mass flow rate between 3 kg/s to 10 kg/s for these heat exchangers. The results showed that the heat transfer and pressure drop of the double shell side rod baffle heat exchanger are higher than single shell side rod baffle heat exchanger. On the other hand, the heat transfer coefficient per pressure drop of double shell side rod baffle heat exchanger is higher than the single shell side rod baffle heat exchanger. Bhutta et al. (2012) prepared a review on CFD applications in heat exchangers. They suggested that CFD is a effective tool for predicting performance and characteristic of heat exchanger. On the other hand, k-ε turbulence model has been mostly used for heat exchangers. Zhang, He, & Tao (2009b) they achieved the 3D numerical simulation on shell and tube heat exchanger with middle overlapped helical baffles using the GAMBIT 2.3 and FLUENT 6.3 softwares. Three different helix angles which is 30°, 40°, and 50° were used, and also continuous helical baffle type heat exchanger is compared with non-continuous helical baffle type heat exchanger according to pressure drop, pressure gradient, shell side heat transfer coefficient, Nusselt number, and shell side heat transfer coefficient per unit pressure drop. This study results show that the shell side heat transfer coefficient per pressure drop, and Nusselt number of the 40° helix angle case is the largest. Thus 40° helix angle possess the best performance. The pressure drop of the heat exchanger model with continuous baffle is 31-46% higher than that the non-continuous baffle of heat exchanger model. The shell side heat transfer coefficient of the continuous model is lower than that the non-continuous baffle of the

heat exchanger model. Maakoul et al. (2017) investigated the design and the thermo-hydraulic performance of a double pipe heat exchanger with helical baffles in the annulus side to obtain numerically. 3D model of this heat exchanger was performed using FLUENT to specify the annulus side flow, heat transfer coefficient of this side, and the pressure drop for different configurations. Numerical analysis is conducted for different values of Reynolds number and baffle spacing. The results of this study showed that helically baffled annulus side enhanced heat transfer performance however high pressure drop compared to the simple double pipe heat exchanger. Shahril et al. (2017) developed a numerical model for shell and double concentric tube heat exchanger (SDCTHEX) using CFD software of FLUENT. A comparison study was conducted for SDCTHEX and classical shell and tube heat exchanger for their thermo – hydraulic performance (heat transfer, pressure drop) for different mass flow rate of shell side fluid. In addition the effect of the inner diameters on the performance of SDCTHEX were showed. The results of the numerical study showed that the SDCTHEX has a higher heat transfer performance whereas lower pressure drop. Jayakumar et al. (2008) developed a 3D numerical model for helical coiled heat exchanger. They specified the heat transfer characteristics inside a helical coil for various boundary conditions. Their study results showed that based on the CFD results, and experimental results a correlation was obtain to generalize various coil configurations. Lei et al. (2008) studied the heat transfer characteristics of a heat exchanger with single helical baffles experimentally as well as numerically. The comparisons of the performance of three heat exchangers with single segment baffle, single helical baffle, and two layers baffles were presented. Their study results show that the heat exchanger with helical baffles have higher heat transfer coefficient to the same pressure drop than that of the heat exchanger with segmental baffles, and two layer helical baffles has better performance than that of the single helical baffle. Nakaso, Mitani, & Fukai (2015) investigated convection heat transfer coefficient of shell and tube heat exchanger with sheet fins using numerical solution method. The heat transfer rate was formulated and includes contact resistance and fin efficiency. This study results show that when sheet fins were used, the pressure drop increased by 10-15%, on the other hand the overall heat transfer coefficient increased by 15-50% with using fins. Because of the increase of the heat transfer surface area. This method

which is used fins in the heat exchanger increases energy efficiency as according to author's comment. Taher et al. (2012) conducted 3D numerical simulation of helical baffled shell and tube heat exchanger to study the effect of baffle spacing on the heat transfer performance of the heat exchanger. Simulations were done for different mass flow rates, and different baffle spacing. Their study results showed that the baffle spacing have significant effect on the helical baffled shell and tube heat exchanger performance. Hosseini, Rahimi, & Bahrampoury (2014) investigated thermal and heat transfer characteristics of the shell and tube heat exchanger as a PCM (phase change material) thermal storage system numerically as well as experimentally. Their study is observed that when the inlet temperature of heat transfer fluid increases, the theoretical efficiency of the heat exchanger both charging and discharging processes. Tan et al. (2013) investigated the fluid and heat transfer characteristics of shell side of twisted oval tube shell and tube heat exchanger to study numerically with realisable k-ε method. They studied parametrically by changing pitch length and aspect ratio. It was observed that Nusselt number and friction factor both increase with the increasing of pitch length and aspect ratio. Singh and Kumar (2014) considered shell and tube heat exchanger to find the pressure, velocity and temperature distribution of this heat exchanger, they conducted numerical analysis. In addition they validated this model with experimental data.

2.6.2 Modelling of Organic Rankine Cycle

In this section, an overview of the modelling of the organic Rankine cycle, an introduction to thermal modelling of subcritical ORC (organic Rankine cycle), and supercritical ORC are given.

There are some studies about subcritical ORCs and their components. Heberle and Brüggemann (2010) studied the concepts of serial and parallel circuits of ORC. The fluid selection was conducted according to the operating parameters. These parameters are geothermal water inlet temperature and supply temperature of the heating system. The results of this study showed that for the serial case of ORC, isobutane is suitable working fluid; whereas for the parallel case, isobutane and R227ea are favourable fluid

types. Zhang et al. (2017) used three different heat exchangers which are plate heat exchanger, shell and tube heat exchanger, and finned tube heat exchanger in the ORC system to investigate the ORC cycle performance comparatively. They obtained the optimal evaporating pressure, pinch point temperature difference, net power output, and dynamic payback period corresponding to the minimum electricity cost. The results showed that the electricity production cost of both evaporator and condenser using plate heat exchanger is the highest. Wang et al. (2012) conducted a mathematical model for subcritical ORC. They presented the selection of working fluid and a parametric optimization using simulated annealing method. The results of their study showed that R123 is the best choice for the temperature range 100-180°C; whereas R141b is the suitable fluid for the temperature higher than 180°C.

There are some studies about the design and modelling of supercritical ORC and their components. Wang et al. (2017) proposed a regenerative supercritical and subcritical dual loop ORC system. A mathematical model was employed to analyze the performance of the system. The performance parameters are the overall cycle efficiency and the net power. In addition, they presented the effects of regeneration and operational parameters such as turbine inlet pressure and temperature on the performance of the supercritical loop. The results of this study showed that dual loop ORC system achieved higher performance than the traditional ORC systems. Dong et al. (2017) presented the thermodynamic analysis of ORC including the working fluid selection and determination of cycle parameters which are cycle efficiency and net power output of the cycle. They found that Siloxane MM is appropriate working fluid for high temperature ORC system. Turbine inlet temperature is found to be more dominant than the inlet pressure of the turbine on the ORC cycle efficiency. In addition, they investigated the radial turbine design through numerical modeling. Hsieh et al. (2017) experimentally examined a 20 kW supercritical ORC with a screw turbine and working fluid as R218 in order to investigate the system performance at the heat source temperature of 90-100°C in both subcritical and supercritical conditions. Shengjun et al. (2011) conducted a thermodynamic and economic performance of both subcritical and supercritical ORC systems for low temperature geothermal power plant (i.e. 80-100°C). In addition, they compared and analyzed the

both system performance under the same operating conditions. They found that R123 as working fluid in subcritical ORC yields the highest performance; whereas R125 in supercritical ORC cycle showed good economic and environmental performance. Vetter et al. (2013) presented and simulated thermodynamic analysis of ORC for power generation using low temperature geothermal wells. They discussed the effect of the geothermal brine inlet temperature on the performance of both subcritical and supercritical ORCs. They found that using propane achieved higher performance compared to CO_2.

2.6.3 Hybrid Solar – Geothermal and Other Hybrid Technologies

Hybridization of power plants is an interesting way to produce more power and has some environmental and economic advantages. There are several studies in literature on the thermal modelling and analyses of hybrid power plants. Tempesti and Fiaschi (2013) conducted a thermo-economic analysis of a micro-ORC system integrated with solar collectors. The thermo-economic performance of three different working fluids (e.g. R134a, R236fa, and R245fa) were compared. The economic analysis showed that R245fa is the most convenient fluid as it allowed the lowest price electricity production and lowest overall cost of the plant. Marion et al. (2012) proposed a mathematical model for subcritical ORC integrated with the solar-thermal collector, when R134a, R227ea and R365mfc are used as the working fluid. The power output of the system was calculated. The pump and turbine efficiencies and the residual collector losses were taken into account in the calculations. Their results showed that the net power output depends on the fluid mass flow rate and the optimum flow as a linear function of the solar radiation. Higher performance is obtained with the R365mfc as the working fluid; ORCs operating with R134a and R227ea follows it, respectively. Kosmadakis et al. (2016) presented a detailed experimental investigation of a small-scale subcritical ORC with the working fluid as R404A. They performed energy and exergy analyses, and focused on the main ORC components. The experimental tests were first conducted at laboratory conditions for finding the design conditions of the main components. The ORC system was coupled with PV/T collectors, which produce electricity and heat that are provided to the ORC. The most important result of

laboratory tests is that only 3 kW capacity ORC system can achieve sufficient thermal efficiency when working at very low temperature. Lazova et al. (2016) designed a supercritical helical coil heat exchanger, then tested it under real operational conditions. Three heat transfer correlations for different working fluids, which were found from the literature, were used. Then, a 3 kW small–scale ORC was integrated with a concentrated solar power technology for electricity generation. The results from this study showed that for better estimation of the sizing of the heat exchanger a more accurate correlation is required in order to design an optimal configuration and thus employ cheaper components. Cakici, Erdogan, & Colpan (2016) assessed the thermodynamic performance of an integrated geothermal powered supercritical regenerative Rankine cycle and parabolic trough solar collectors (PTSCs). A thermal model is developed for overall integrated system and its components. This model gives the performance assessment parameters of the system which are the electrical and exergetic efficiencies, total exergy loss and destruction, productivity lack, fuel depletion ratio, and improvement potential rate. The model is validated according to existing supercritical based power plant, and literature data for PTSC. The results show that integration ORC and PTSC systems increase the net power output however decrease the electrical and exergetic efficiencies. It was also shown that R134a is the most suitable fluid for this system.

CHAPTER THREE
DESIGN AND MODELING OF SOLAR – GEOTHERMAL HEAT EXCHANGERS

3.1 Introduction

In this chapter, the design and modeling techniques and equations of shell and tube heat exchanger and parabolic trough solar collectors, and its solution methodologies are given. Firstly, the general description of the system is given. Secondly, the analytical and numerical modeling equations of shell and tube heat exchangers, and the solution procedures are examined. Finally, the modeling equations for parabolic trough solar collectors are presented.

3.2 System Description

The process flow diagrams of integrated geothermal powered ORC and PTSCs systems modeled in this study are shown in Figure 3.1. As can be seen in this figure, the operating principle of the ORC system is as follows. The geothermal brine extracted from production well enters the shell side of the heat exchanger. Here, it transfers its heat to the ORC working fluid. On the other hand, working fluid of the ORC system enters from the tube side of the heat exchanger. Depending on the cycle configuration, the working fluid exiting the tube side of the heat exchanger is at either subcritical or supercritical state. Then, the working fluid enters the turbine where the power is produced. After it leaves the turbine, it enters the desuperheater, which is used to increase the electrical efficiency of the ORC systems by increasing the temperature of the working fluid entering the heat exchanger. Working fluid exiting the desuperheater enters the air cooled condenser (ACC) and leaves as saturated liquid. As it exits the ACC, it enters the pump; then it enters the desuperheater and the heat exchanger again to complete the cycle. On the other side, the geothermal brine exiting the heat exchanger is sent back to reinjection well in order to ensure the sustainability of the geothermal resource. In this thesis, a design study for shell and tube heat

exchangers which are shown with dashed line in Figure 3.1, and the parabolic trough solar collectors is conducted.

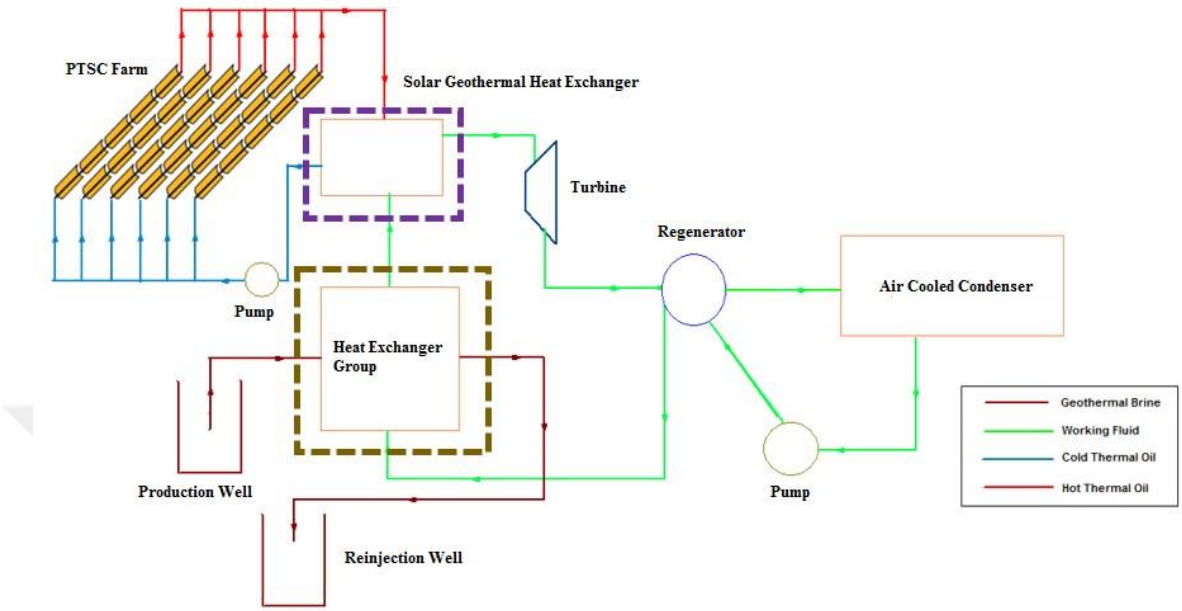

Figure 3.1 The schematic of the hybrid solar – geothermal power plant

3.3 Analytical Modeling of Shell and Tube Heat Exchanger

In this section, the analytical equations for shell and tube heat exchanger and the solution procedure are presented.

3.3.1 Governing Equations for Shell and Tube Heat Exchangers

A design problem, in which the inlet and exit conditions of the PTSC side (shell side of the heat exchanger) and the inlet condition of the ORC side (tube side of the heat exchanger) are known, is considered in the modeling of a shell and tube heat exchanger. Using the model developed, the overall heat transfer coefficient, the heat transfer surface area, the pressure drop across the heat exchanger, and the required pumping power are found. The following main assumptions are made in this model.

- The heat exchanger runs under steady-state conditions.

- Heat losses from the outer surface of the heat exchanger to the surroundings are negligible.
- The temperature of each fluid at the inlet and exit is uniform across the cross-sectional areas of the shell and the tube.
- Thermo-physical properties are evaluated at an average value of temperature between the inlet and outlet streams.
- Changes in the kinetic and potential energies of the flowing streams between the inlet and exit can be neglected.
- The temperature change of the fluid between the inlet and exit of the pump is neglected.
- The pressure drop across the tube side of the heat exchanger is ignored.

First of all, the heat transfer rate between the hot and cold streams is found using Eq. (3.1). Then, the specific enthalpy of the cold fluid outlet ($h_{c,o}$) can be found applying an energy balance around the cold stream part of the heat exchanger as shown in Eq. (3.2).

$$\dot{Q}_{hx} = \dot{m}_h \cdot \left(h_{h,i} - h_{h,o}\right) \tag{3.1}$$

$$h_{c,o} = h_{c,i} + \frac{\dot{Q}_{hx}}{\dot{m}_c} \tag{3.2}$$

Overall heat transfer coefficient can be calculated as follows.

$$\frac{1}{U} = \frac{D_o}{D_i}\frac{1}{h_i} + \frac{\ln(D_o/D_i)}{2\pi kL} + \frac{1}{h_o} + \frac{D_o}{D_i}R"_{fi} + R"_{fo} \tag{3.3}$$

Fouling factors ($R"_f$) at the tube and shell sides given in Eq. (3.3) are taken as 0.0002 $m^2 \cdot K/W$ in this study (Kakaç, Liu, & Pramuanjaroenkij, 2002).

To calculate the heat transfer coefficient of the tube side (h_i) given in Eq. (3.5), which is a function Nusselt number (Nu), the thermal conductivity of the ORC fluid, and the inner diameter of the tube (D_i), Reynolds number should be first calculated as shown in Eq. (3.4).

$$Re = \frac{4 \cdot \dot{m}_c}{\mu \cdot \pi \cdot D_i \cdot \frac{N_T}{n_{pass}}} \tag{3.4}$$

After calculating the Reynolds number, Nusselt number can be found according to the relevant phase and regime.

For single phase flow:

$$Nu = \frac{h_i D_i}{k} = 4.36 \text{ (For } Re \leq 2300) \tag{3.5}$$

$$Nu = \frac{h_i D_i}{k} = \frac{\frac{f}{8}(Re - 1000)Pr}{1 + 12.7\left(\frac{f}{8}\right)^{\frac{1}{3}}(Pr^{\frac{2}{3}} - 1)} \text{ (For } 2300 < Re < 5x10^4) \tag{3.6}$$

The boiling heat transfer coefficient for two phase flow is calculated by Kandlikar equation (Kandlikar, 1990).

$$h_{tp} = h_{liq} \cdot \left(C_1 \cdot Co^{C_2} \cdot (25 \cdot Fr)^{C_5} + C_3 \cdot Bo^{C_4} \cdot F_{fl}\right) \tag{3.7}$$

Where Co, Fr, and Bo are Convection number, Froude number, and Boiling number respectively, and can be found as follows.

$$Co = \left(\frac{1-x}{x}\right)^{0.8} \cdot \left(\frac{\rho_g}{\rho_l}\right)^{0.5} \tag{3.8}$$

$$Bo = \frac{\dot{Q}}{\dot{m} \cdot \Delta h_{vap}} \tag{3.9}$$

$$Fr = \frac{\left(\frac{\dot{m}}{A}\right)^2}{\rho^2 \cdot g \cdot D_i} \tag{3.10}$$

F_{fl} given in Eq. (3.7) is the fluid – dependent parameter and can be found in Kakaç et al. (2002) and Kandlikar (1990). C_1 – C_5 constants given in Eq. (3.7) are given in Table 3.1.

Table 3.1 Constants in Kandlikar equation (Kandlikar, 1990)

Constants	**Convective Boiling Region (Co<0.65)**	**Nucleate Boiling Region (Co>0.65)**
C_1	1.1360	0.6683
C_2	-0.9	-0.2
C_3	667.2	1058
C_4	0.7	0.7
C_5	0.3	0.3

To calculate the heat transfer coefficient of the shell side (h_o), Nusselt number should be first calculated using the equation developed by McAdams (Kakaç, Liu, & Pramuanjaroenkij 2002), which is shown in Eq. (3.11).

$$\mathrm{Nu} = \frac{\mathrm{h_o \cdot D_e}}{\mathrm{k}} = 0.36 \cdot \mathrm{Re}^{0.55} \cdot \mathrm{Pr}^{\frac{1}{3}} \cdot \left(\frac{\mu_\mathrm{b}}{\mu_\mathrm{w}}\right)^{0.14} \tag{3.11}$$

In Eq. (3.11), equivalent diameter (D_e) depends on the layout angle as shown in Eqs. (3.12) and (3.13) (Kakaç, Liu, & Pramuanjaroenkij, 2002). Here, P_t is the tube pitch, which changes according to the tube diameter (Harrison, 2007). The schematic of the pipe alignments for different layout angles is given in Figure 3.2.

$D_e = \frac{1.27}{D_o}\left({P_t}^2 - 0.785 \cdot {D_o}^2\right)$ (For triangular pipe alignment, 30° or 60° layout angle) (3.12)

$D_e = \frac{1.10}{D_o}\left({P_t}^2 - 0.917 \cdot {D_o}^2\right)$ (For square pipe alignment, 45° or 90° layout angle) (3.13)

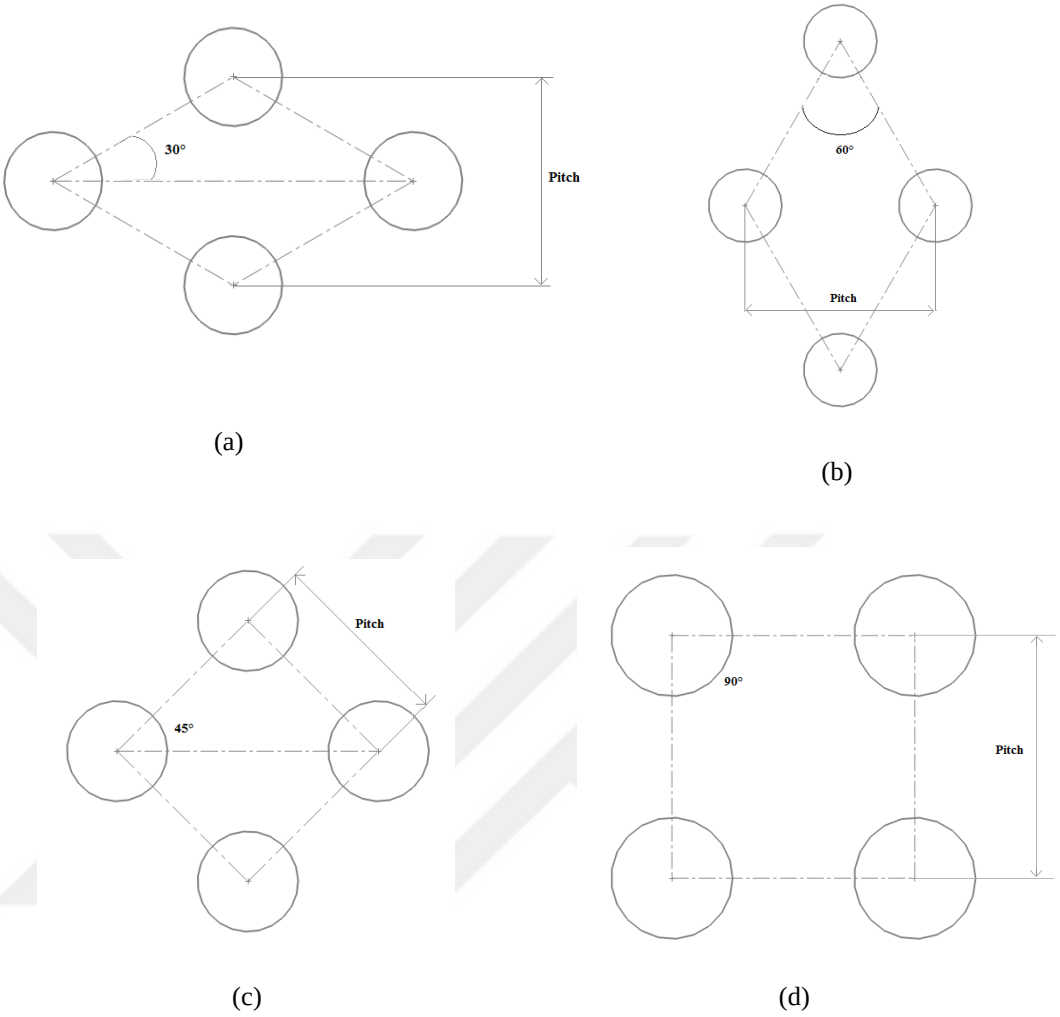

Figure 3.2 The schematic of the pipe alignments for different layout angles: (a) 30°, (b) 60°, (c) 45°, and (d) 90°

Reynolds number of the shell side can be given using Eq. (3.14). In this equation, the cross sectional area of the shell perpendicular to the flow direction, A_s, can be found according to different baffle configurations using Eq. (3.15) (Kakaç, Liu, & Pramuanjaroenkij, 2002). The schematics of baffle configuration types are shown in Figure 3.3.

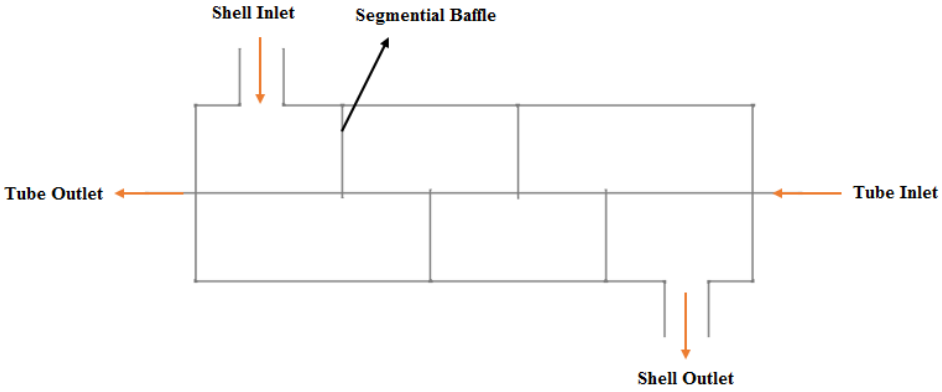

(a)

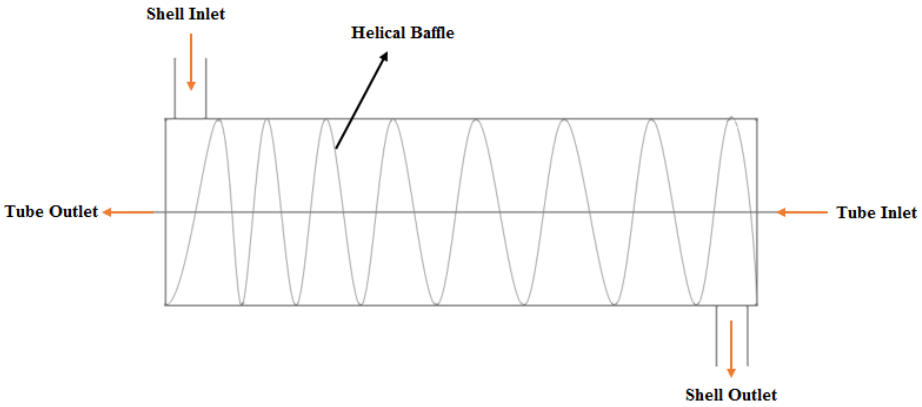

(b)

Figure 3.3 The schematics of different baffle type of shell and tube heat exchangers (a) segmental baffle (b) helical baffle

$$\mathrm{Re}_{shell} = \frac{\mathrm{D_e}\cdot \dot{m}_h}{\mu \cdot \mathrm{A_s}} \tag{3.14}$$

$$A_s = 0.639(P_t - D_o) \cdot e \cdot \sqrt{\frac{CL}{CTP} \cdot \pi \cdot N_T} \tag{3.15}$$

$$A_s = 0.5 \cdot e \cdot \left[D_{shell} - D_{otl} + \frac{D_{otl} - D_o}{P_t} \cdot (P_t - D_o)\right] \text{ (For continuous and non-continuous baffle configurations)} \tag{3.16}$$

Here, e is baffle spacing, and calculated using Eqs. (3.17) and (3.18) for continuous and non-continuous baffle configurations, respectively.

$$e = \pi \cdot D_{shell} \cdot \tan\beta \text{ (For continuous baffle configuration)} \tag{3.17}$$

$$e = \sqrt{2} \cdot D_{shell} \cdot \tan\beta \text{ (For non-continuous baffle configuration)} \tag{3.18}$$

Tube layout constant (CL) and tube count calculation constant (CTP) depend on the geometry of heat exchanger as shown in Table 3.2.

Table 3.2 CL and CTP values (Kakaç, Liu, & Pramuanjaroenkij 2002)

Tube Layout Angle	**CL**
For 90^o and 45^o	1
For 30^o and 60^o	0.85
Number of Passes	**CTP**
One Pass	0.93
Two Passes	0.9
Three Passes	0.85

Using LMTD method for a counter flow type heat exchanger, the number of tubes can be calculated using Eq. (3.19). In this equation, F is the correction factor, which can be found using the figures given in Ref. (Kakaç, Liu, & Pramuanjaroenkij, 2002).

$$N_T = \frac{\dot{Q}_{hx}}{U \cdot F \cdot \left[\frac{(T_{h,i}-T_{c,o})-(T_{h,o}-T_{c,i})}{\ln\frac{(T_{h,i}-T_{c,o})}{(T_{h,o}-T_{c,i})}}\right] \cdot \pi \cdot D_o \cdot L \cdot n_{pass}} \tag{3.19}$$

After finding the length of the zone using iterative solutions, the heat transfer surface area of each zone is calculated using Eq. (3.20).

$$A = \pi D_o L N_T n_{pass} \tag{3.20}$$

The pressure drop between the shell and tube sides of each inlet and exit streams can be found according to the relevant phase as follows.

For single phase (Kakaç et al., 2002):

$$\Delta P_{tube} = 4 \cdot \exp[0.576 - 0.19 \ln(\mathrm{Re}_{\mathrm{shell}})] \cdot L_{zone} \cdot \frac{n_{pass}}{D_i} + 4 \cdot n_{pass} \cdot \frac{\rho \cdot V^2}{2} \tag{3.21}$$

For two phase region (Ishiharaa et al., 1980):

$$\Delta P_{tube} = \frac{2 \cdot f_{tp} \cdot \frac{\dot{m}}{A} \cdot L_{zone} \cdot v_f}{D_i} \cdot \left(1 + \frac{x \cdot (v_g - v_f)}{2 \cdot v_f}\right) \tag{3.22}$$

For supercritical region (Fang et al., 2012):

$$\Delta P_{tube} = \frac{2 \cdot f_s \cdot \frac{\dot{m}}{A} \cdot L_{zone}}{2 \cdot \rho \cdot D_i} \tag{3.23}$$

Where f_s is the supercritical phase friction factor and can be found using Eq. (3.24).

$$f_s = f_{iso} \cdot \left(\frac{\mu_w}{\mu_b}\right)^{0.49 \cdot \left(\frac{\rho_b}{\rho_f}\right)^{1.31}} \tag{3.24}$$

In this equation f_{iso} is the isothermal single phase friction factor and can be found using Eq. (3.25).

$$f_{iso} = 1.613 \cdot \left(\ln\left(0.234 \cdot \left(\frac{\varepsilon}{D_i}\right)^{1.1007} - \frac{60.525}{Re^{1.1105}} + \frac{56.291}{Re^{1.0712}}\right)\right)^{-2} \tag{3.25}$$

The shell side pressure drop can be found using Eq. (3.26) for single phase region (Kakaç et al., 2002).

$$\Delta P_{shell} = \frac{f_{fric} \cdot G_{shell}^2 \cdot \left(\left(\frac{L}{e}+1\right)+1\right) \cdot D_{shell}}{2 \cdot \rho \cdot D_e \cdot \left(\frac{\mu_b}{\mu_w}\right)^{0.14}} \tag{3.26}$$

Where G_{shell} is the mass velocity of shell side fluid, N_b is the number of baffles, f_{fric} is the friction factor and φ_{shell} is the viscosity ratio between bulk and wall temperatures. These parameters can be calculated as follows (Shah & Sekulic, 2002).

$$f_{fric} = \exp[0.576 - 0.19 \cdot \ln(Re_{shell})] \tag{3.27}$$

$$G_{shell} = \frac{\dot{m}_h}{A_s} \tag{3.28}$$

$$\varphi_{shell} = \left(\frac{\mu_b}{\mu_w}\right)^{0.14} \tag{3.29}$$

$$N_b = \left(\frac{L}{e} + 1\right) \tag{3.30}$$

3.3.2 Numerical Solution for Shell and Tube Heat Exchanger

In this study the modeling equations, which is given above, were entered and were solved using Engineering Equation Solver (EES). For this purpose, an iterative solution method is applied to find the number of tubes in this study. In this method, an initial guess for the number of tubes found in the heat exchanger is first made. Using this initial guess, the equations given above (Eqs. (3.3)-(3.18)) and the relations and data are solved to find the overall heat transfer coefficient (U). Using the value of this coefficient, Eq. (3.19) is solved to find the number of tubes again. The iterations continue until the absolute value of the difference between the initial guess and the number of tubes found from Eq. (3.19) is smaller than a threshold value (e.g. 10^{-4}). After finding the number of tubes, the heat transfer surface area can be found using Eq. (3.20). To better understand the solution methodology, the flow chart of the heat exchanger model is given in Figure 3.4.

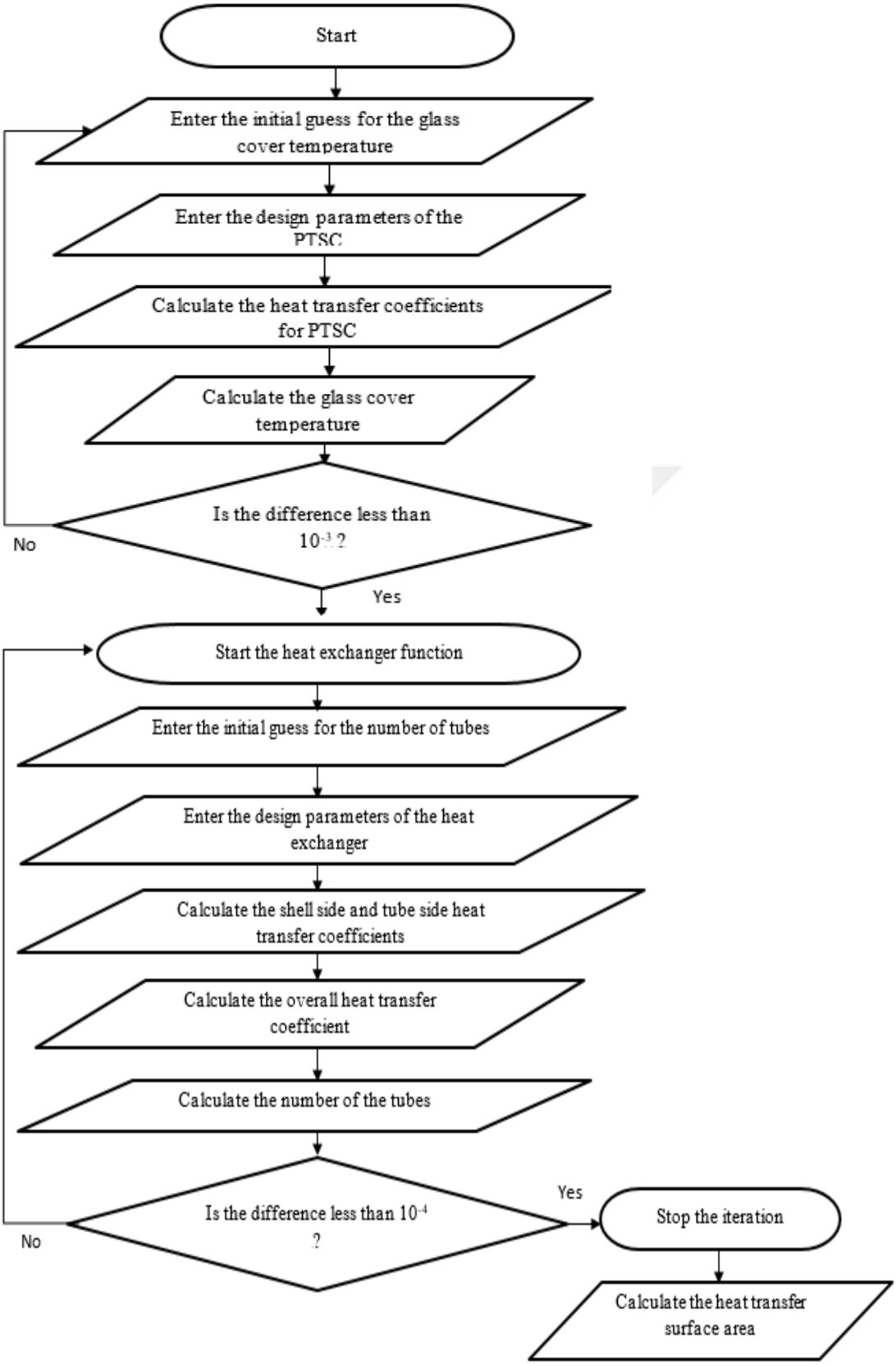

Figure 3.4 Flow chart of calculation process

3.4 CFD Modeling of Shell and Tube Heat Exchanger

3.4.1 Governing Equations

To model the 3D shell and tube heat exchanger (STHX), the following assumptions were considered:

- The heat exchanger operates under steady state conditions.
- The shell walls are well-insulated (adiabatic)
- Both working fluids are Newtonian and their thermophysical properties are taken as constant.
- The shell-side and the tube side flows are turbulent and can be modeled using the realizable k-ε model
- The baffles and tube walls are sufficiently thin to be treated as interfaces imposing a conductive thermal resistance to the flow.
- Viscous heating and pressure force effects are neglected.

Considering these assumptions, the hydrodynamics of the heat exchanger is modeled using the conservation of mass, momentum, energy, kinetic energy and energy dissipation equations; the realizable k-ε model. These equations are provided in this section (COMSOL User's Guide, 2015; Patankar, 1980). To begin the discussion, the flow field's mean velocity, pressure and temperatures are calculated from the conservation of mass, momentum and energy, given by Eqs. (3.31) to (3.33), shown below.

$$\rho(\nabla \cdot \mathrm{u}) = 0 \tag{3.31}$$

$$\rho \mathrm{u}(\nabla \cdot \mathrm{u}) = \nabla \cdot \left[-p\mathrm{I} + \mu_{eff}(\nabla \mathrm{u} + (\nabla \mathrm{u})^{\mathrm{T}}) - \frac{2}{3}\rho k \mathrm{I}\right] \tag{3.32}$$

$$\rho \mathrm{u} c_p(\nabla T) = \nabla \cdot \left[\lambda_{eff}(\nabla T)\right] \tag{3.33}$$

Here, ρ is the fluid's mass density, u is the fluid's velocity vector, p is the pressure, I is the identity matrix, μ_{eff} is the effective (intrinsic plus turbulent) dynamic

viscosity, *k* is the turbulent kinetic energy, c_p is the specific heat at constant pressure, *T* is the temperature, and λ_{eff} is the effective (intrinsic plus turbulent) thermal conductivity. The effective dynamic viscosity and thermal conductivity are given by Eqs. (3.34) and (3.35). The subscripts *l* and *t*, in these equations, refer to the liquid state and turbulent properties, respectively.

$$\lambda_{eff} = \lambda_l + \lambda_t \tag{3.34}$$

$$\mu_{eff} = \mu_l + \mu_t \tag{3.35}$$

The turbulent thermal conductivity and dynamic viscosity are obtained from the Kays-Crawford equation and the k-ε model, respectively. The turbulent Prandtl number at infinity, Pr_{T_∞}, is taken as 0.85 (Patankar, 1980)

$$Pr_T = \frac{C_p \mu_T}{\lambda_T} = \left[\frac{1}{2 \cdot Pr_{T_\infty}} + \frac{0.3}{\sqrt{Pr_{T_\infty}}}\frac{C_p \mu_T}{\lambda} - \left(0.3\frac{C_p \mu_T}{\lambda}\right)^2 \left(1 - exp\left(-\frac{\sqrt{Pr_{T_\infty}}}{0.3}\frac{\lambda}{0.3 C_p \mu_T}\right)\right)\right]^{-1} \tag{3.36}$$

$$\mu_T = \rho C_\mu \frac{\mathrm{k}^2}{\varepsilon} \tag{3.37}$$

To determine the fluids' turbulent kinetic energy, k, and energy dissipation, ε, the following equations are applied.

$$\rho \mathrm{k}(\mathrm{u} \cdot \nabla) = \nabla \cdot \left[\left(\mu + \frac{\mu_T}{\sigma_K}\right)(\nabla \mathrm{k})\right] + P_k - \rho\varepsilon \tag{3.38}$$

$$\rho \varepsilon(\mathrm{u} \cdot \nabla) = \nabla \cdot \left[\left(\mu + \frac{\mu_T}{\sigma_\varepsilon}\right)(\nabla \varepsilon)\right] + C_{\varepsilon 1}\frac{\varepsilon}{k}P_k - C_{\varepsilon 2}\rho\frac{\varepsilon^2}{k} \tag{3.39}$$

The k-ε model constants (C_μ,$C_{\varepsilon 1}$, $C_{\varepsilon 2}$, σ_K, and σ_ε) are summarized in Table 2, whereas the turbulent kinetic energy production rate, P_k, is calculated using Eq. (3.40).

$$P_k = \mu_T \left[(\nabla \mathrm{u}) : \left((\nabla \mathrm{u}) + (\nabla \mathrm{u})^{\mathrm{T}}\right) - \frac{2}{3}(\nabla \cdot \mathrm{u})^2\right] - \frac{2}{3}\rho \mathrm{k}(\nabla \cdot \mathrm{u}) \tag{3.40}$$

The velocity inlets of the tubes and shells were specified with a known mass flow rates, $\dot{m}_{inlet}$. The kinetic energy and energy dissipation at the inlets, are calculated based off of the flow's incoming turbulence intensity, I_T (considered to be 0.05). And the energy equation is treated with a constant and known inlet temperature, T_0. These conditions are given by Eqs. (3.41) - (3.44) respectively.

$$\dot{m}_{inlet} = \int \rho(\mathrm{u}_{\mathrm{inlet}} \cdot \mathrm{n}) dA \tag{3.41}$$

$$k_{inlet} = \frac{3}{2}(|\mathrm{u}|I_T)^2 \tag{3.42}$$

$$\varepsilon_{inlet} = C_\mu^{3/4} \frac{k_{inlet}^{3/2}}{L_T} \tag{3.43}$$

$$T_{inlet} = T_0 \tag{3.44}$$

Here, n is the normal vector, A is the surface area, and L_T is the turbulence length scale (considered to be 0.01 m). The outlets are treated with a specified zero-gauge pressure boundary condition, P_{outlet}, and standard outlet (convective) boundary conditions; given by Eqs. (3.45) - (3.46). Here ϕ is an arbitrary variable (i.e.: energy dissipation, kinetic energy, stress, and temperature). The symmetry condition on the mid-plane of the heat exchanger, as shown in Fig. 3, uses the same form of boundary condition shown in Eq. (3.46).

$$\left[-p\mathrm{I} + \mu_{eff}(\nabla\mathrm{u} + (\nabla\mathrm{u})^{\mathrm{T}}) - \frac{2}{3}\rho k\mathrm{I}\right]_{outlet} \cdot \mathrm{n} = 0 \tag{3.45}$$

$$(\nabla\phi) \cdot \mathrm{n} = 0 \tag{3.46}$$

All walls (shell, tube and baffles) were specified with no slip for smooth walls, and impermeable wall conditions, as given by Eqs. (3.47) - (3.48).

$$\mathrm{u} \cdot \mathrm{n} = 0 \tag{3.47}$$

$$\left[-p\mathrm{I} + \mu_{eff}(\nabla\mathrm{u} + (\nabla\mathrm{u})^{\mathrm{T}}) - \frac{2}{3}\rho k\mathrm{I}\right]\mathrm{n} = -\rho\frac{u_\tau}{\delta_w^+}\mathrm{u}_{\mathrm{tang}} \tag{3.48}$$

The corresponding stress, given by the right hand side of Eq. (3.48), is composed of the friction velocity, u_τ, the non-dimensional position normal to the wall's surface,

δ_w^+, and the tangential velocity, $\mathrm{u_{tang}}$. The u_τ and δ_w^+ are obtained from standard wall functions (which is also true for all quantities near-wall), whereas $\mathrm{u_{tang}}$ is obtained from Eq. (3.49).

$$\mathrm{u_{tang}} = \mathrm{u} - (\mathrm{u} \cdot \mathrm{n})\mathrm{n} \tag{3.49}$$

3.4.2 Numerical Solution

In this study, COMSOL Multiphysics® 5.0, a commercially available finite element solver, is used to solve the equations discussed Section 3.4.1. After entering all the necessary equations using the software's built-in modules ("Turbulent Flow, k-ε", and "Heat Transfer in Fluids"), the mesh was generated for the geometry. Tetrahedral elements are used to mesh the shell and tubes, with increase resolution imposed at the walls to capture the hydraulic boundary layers. A total of ~8.5 million elements are used to mesh the geometry in this study. Three different segregated groups (pressure and velocity [P and **u**], temperature [T], and kinetic energy [k] and energy dissipation [ε]) are setup to solve each set of the equations, each using the multifrontal massively parallel sparse (MUMPS) direct solver. The solution progressed until the residuals fell below 10^{-4}.

To ensure a robust solution, under-relaxation is applied to each segregated step, and the kinetic energy and energy dissipation variables are considered to be greater than zero. Furthermore, to prevent excessive turbulence production in the limit where $k \rightarrow 0$ (see Eq. (9)), a mixing length limiter was introduced, as given by Eqs. (3.50) and (3.51). Here, $l_{mix,max}$ is the maximum mixing length and **S** is the strain rate vector, given by Eq. (3.52). The derivation of this limiter is provided in Patankar, (1980).

$$l_{mix} = max\left(C_\mu \frac{\mathrm{k}^{1/2}}{\varepsilon}, l_{mix,max}\right) \tag{3.50}$$

$$l_{mix,max} \leq \sqrt{\frac{k}{6(\mathbf{S}\cdot\mathbf{S})}} \tag{3.51}$$

$$\mathrm{S} = \frac{1}{2}[(\nabla \mathrm{u}) + (\nabla \mathrm{u})^T] \tag{3.52}$$

3.5 Mathematical Modelling of Parabolic Trough Solar Collectors

In this section, the modeling approach and equations for the PTSC are given. The aim of the PTSC model developed is to find the exit temperature of the PTSC system for a given set of input parameters consisting of the design and operating parameters of PTSC as well as the meteorological data. Modeling of PTSC discussed in this section is based on the approach and equations given in the Duffie and Beckman, (2013); Kalogirou (2009). The schematic of a PTSC and its layers are shown in Figure 3.5.

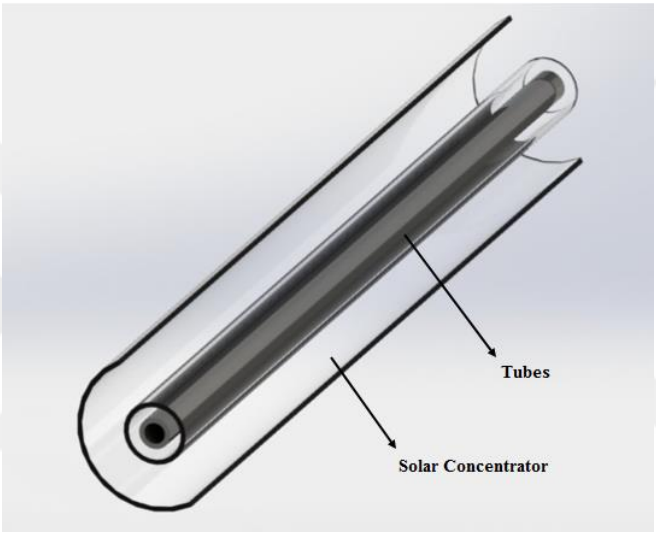

(a)

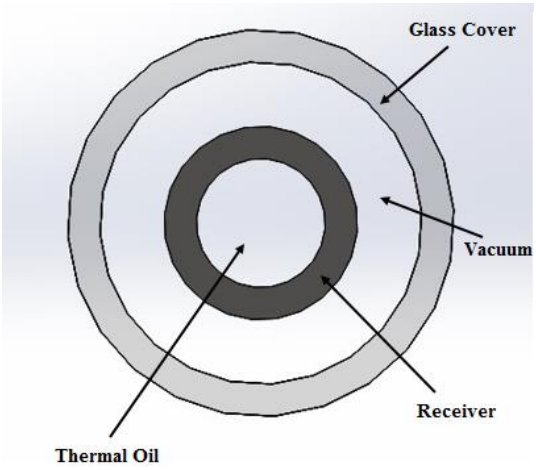

(b)

Figure 3.5 Schematic of (a) the main components of the PTSC and (b) the cross section of the PTSC tubes

The rate of useful energy delivered by a single collector to the PTSC side fluid can be found using Eq. (3.53).

$$\dot{Q}_u = F_R[G_b \rho \gamma \tau \alpha K A_a - A_r U_L (T_i - T_a)] \tag{3.53}$$

Where $G_b$is the solar irradiation intensity, ρ is the reflectance of the mirror, τ is the transmittance of the glass cover, α is the absorptivity, and K is the incidence angle modifier. The heat removal factor is given by Eq. (3.54).

$$F_R = \frac{\dot{m}_h \cdot c_p}{A_r \cdot U_L}\left[1 - exp\left(-\frac{U_L \cdot F' \cdot A_r}{\dot{m}_h \cdot c_p}\right)\right] \tag{3.54}$$

F' is the collector efficiency factor, which can be found using Eq. (3.55).

$$F' = \frac{\frac{1}{U_L}}{\frac{1}{U_L} + \frac{D_o}{h_{fi} D_i} + \left(\frac{D_o}{2k} + \ln\frac{D_o}{D_i}\right)} \tag{3.55}$$

To calculate h_{fi}, which is the heat transfer coefficient of the inside of the receiver tube, Eq. (3.56) can be used.

$$h_{fi} = \frac{Nu \cdot k_{fi}}{D_i} \tag{3.56}$$

Where Nu is the Nusselt number of the fluid flowing through the receiver. If the flow is laminar, (Re<2300) Nusselt number can be taken as constant as 4.364. If the flow inside the receiver tube is turbulent (Re>2300), Nusselt number can be evaluated using the following correlation (Duffie and Beckman, 2013):

$$Nu = 0.023(Re^{0.8})(Pr^{0.4}) \tag{3.57}$$

The solar collector heat loss coefficient can be shown as:

$$U_L = \left(\frac{A_r}{(h_{c,g-a}+h_{r,g-a})A_g}\right)^{-1} \quad (3.58)$$

The equations to calculate $h_{c,g-a}$ and $h_{r,g-a}$ can be found in Duffie and Beckman (2013); Fernández-García et al. (2010); Kalogirou (2004) & (2009). To find these heat transfer coefficients, which are functions of the glass cover temperature, an iterative solution method should be applied. For this purpose, an initial guess for the value of the glass cover temperature (T_g) should be given; and then after calculating the relevant heat transfer coefficients, the value of this temperature should be found using Eq. (3.59).

$$T_g = \frac{A_r h_{r,r-g} T_r + A_g(h_{r,g-a}+h_{c,g-a})T_a}{A_r h_{r,r-g}+A_g(h_{r,g-a}+h_{c,g-a})} \quad (3.59)$$

In Eq. (3.59), the correlation to calculate $h_{r,r-g}$ can also be found in Duffie and Beckman (2013); Fernández-García et al. (2010); Kalogirou (2004), (2009).

To find the exit temperature of the PTSC (or the inlet temperature of the heat exchanger for the shell side), an energy balance around the PTSC should be applied, as shown in Eq. (3.60). In this equation, it is assumed that the thermal oil is an incompressible fluid and the enthalpy difference is only a function of the temperature difference between the inlet and exit of the PTSC (the contribution of the pressure drop along the PTSC in the enthalpy difference is neglected).

$$T_{h,i} = T_{h,o} + \frac{\dot{Q}_u}{\dot{m}_h \cdot c_{p,h}} \quad (3.60)$$

The modeling equations which were given above are entered EES, and then solved. An iteration solution method was applied to find the glass cover temperature. For this purpose, a guess value for glass cover temperature (T_g) is given. If the value of T_g found from this equation is different than the initial guess, the iteration must continue until the difference is below a certain threshold value (e.g. 10^{-3} °C).

CHAPTER FOUR
RESULTS AND DISSCUSSIONS

4.1 Introduction

This chapter includes the results of the shell and tube heat exchanger integrating ORC and PTSC, and integrating ORC and geothermal source system discussed in Section 3. First of all, the design and operating parameters of shell and tube heat exchanger used in ORC and PTSC, and shell and tube heat exchanger used in ORC and geothermal source for baseline conditions are given. Second, the effects of some important design and operating parameters on the performance of the both shell and tube heat exchangers are investigated. The design and operating parameters are tube diameter, tube length, baffle spacing, solar irradiation, working fluid types of ORC, and the source temperature of ORC. The performance parameters are the heat transfer surface area, the pumping power. The modelling equations given in Section 3 are entered and solved, and the parametric studies are conducted using 'Engineering Equation Solver (EES)'. Finally the results of the obtaining from the analyses are presented.

In parametric analysis for effect of tube diameter, other design and operating parameters such as inlet and outlet temperatures and pressures of shell and tube side fluids, mass flow rates of both fluids, and tube length are fixed. As a result of parametric iterations, a new design is obtained by calculating a new number of tubes and tube side heat transfer coefficients depending on each diameter change. On the other hand, in zone modelling of heat exchanger for the diameter of tube, the design and operating parameters including number of tubes, baffle spacing, inlet and outlet temperatures and pressures of each fluids are fixed. When the tube diameter is changed, the zone length is updated thus a new design configuration is obtained. In addition, the geothermal source temperature is changed. For this purpose, the design parameters which are tube diameters, baffle spacing, shell diameter, number of tubes and number of passes are fixed. Thus the shell side and tube side heat transfer coefficients, pressure drop of tube side fluid, the outlet temperature of shell side fluid, and zone length are calculated using iterative solution techniques.

4.2 Case Study

In this thesis, the design study for shell and tube heat exchangers integrating with ORC and PTSC, and also ORC and geothermal source are conducted. For this purpose, the analytical and numerical equations for the shell and tube heat exchanger given in Section 3 are solved using Engineering Equation Solver (EES) which is a commercially available software. Then a parametric study is conducted to specify the shell and tube heat exchanger performance.

The type of the collector selected is SkyTrough® collector ("SkyTrough Next-Generation Solar Parabolic Trough Technology", 2009). The geometric data of this PTSC are given in Table 4.1. In addition to these data, the following input parameters are taken in the modeling of the PTSC. The surface temperature of the receiver (T_r), the inlet temperature of the PTSC side fluid ($T_{h,i}$), the ambient temperature, the solar irradiation intensity, and the ambient pressure are taken as 300°C, 290°C, 25°C, 900 W/m^2, and 101.325 kPa, respectively.

Table 4.1 Geometric data of the SkyTrough® PTSC

Single collectors width	6 m (SkyTrough Fact Sheet, 2015)
Single collectors length	14 m (SkyTrough Fact Sheet, 2015)
Receiver inner diameter	0.080 m (Kerme and Orfi 2015; SkyTrough Fact Sheet, 2015)
Receiver outer diameter	0.090 m (Kerme and Orfi 2015; SkyTrough Fact Sheet, 2015)
Glass cover diameter	0.125 m (SkyTrough Fact Sheet, 2015)
Transmissivity of the receiver	0.94 (Kerme and Orfi, 2015)
Absorptivity of the receiver	0.97 (Kerme and Orfi, 2015)
Reflectivity of the aperture surface	0.96 (Kerme and Orfi, 2015)
Receiver emittance	0.92 (Kerme and Orfi, 2015)
Glass cover emittance	0.87 (Al-Sulaiman, 2014; Kerme and Orfi, 2015)
Intercept factor	0.93 (Al-Sulaiman, 2014)
Incidence angle modifier	1 (Al-Sulaiman, 2014)

For the baseline condition of the simulations for shell and tube heat exchanger integrating PTSC and ORC, one shell and one tube pass type heat exchanger is used in the system shown in Fig. 3.1 with purple dashed line. The input parameters of the heat exchanger model for the baseline conditions are given in Table 4.2. The parametric studies were conducted in a range between the minimum and maximum values for outer diameter of the tube, tube length, and baffle spacing considering the standards given in TEMA (Harrison, 2007). These values are shown in Table 4.3. For the ORC and PTSC side fluids, several possible fluids that are feasible to use in such a system are selected. The number of passes is taken as 1, 2, or 3; whereas the tube layout angle is taken as 30°, 45°, 60°, or 90°.

Table 4.2 Input parameters of the heat exchanger model for the baseline conditions

Name of the parameter	**Value**
PTSC side fluid	Therminol VP1
ORC side fluid	R134a
Number of passes	1
Tube length	12 m
Inner diameter of the tube	0.016 m
Wall thickness	0.0015 m
Tube pitch	0.0254 m
Tube layout angle	90°
Baffle spacing	1.5 m
Thermal conductivity of tube	63.9 W/m·K
Mass flow rate of cold fluid	213.368 kg/s
Mass flow rate of hot fluid	27.5 kg/s
Pressure of the fluid in the ORC side	4370 kPa
Outlet temperature of the hot fluid	290°C
Inlet temperature of the cold fluid	147.7°C

Table 4.3 The range of the values of the design parameters used in the parametric study

	Outer Diameter of the Tube (m)	Tube Length (m)	Baffle Spacing (m)
Minimum	0.0064	2.438	0.08038
Maximum	0.0508	11.58	1.5

For the baseline condition of the simulations for shell and tube heat exchanger integrating ORC and geothermal source, one shell and one tube pass type heat exchanger is used in the system shown in Fig. 3.1 with green dashed line. The input parameters of the heat exchanger model and the ORC input parameters which are subcritical and supercritical for the baseline conditions are given in Table 4.4 and Table 4.5 respectively.

Table 4.4 The input parameters of the heat exchanger model for the baseline conditions

Parameters	**Values**
Shell side fluid	Geothermal water
Tube (ORC) side fluid	R134a
Number of pass	1
Number of tubes	1000
Inner diameter of tube (m)	0.016
Baffle spacing (m)	0.5
Tube pitch (m)	0.0254
Mass flow rate of shell side fluid (kg/s)	120.7
Mass flow rate of tube side fluid (kg/s)	213.4
Thermal conductivity of tube (W/m·K)	63.9

Table 4.5 Input parameters of the subcritical and supercritical ORC for the baseline conditions

Common Parameters	
The mass flow rate of air in the ACC (kg/s)	3240
The fan power in the ACC (kW)	600
The generator efficiency	98%
The isentropic efficiency of the turbine	80%
The pressure of the condenser (kPa)	947
The pressure of geothermal water entering the heat exchanger (kPa)	624.8
The temperature of geothermal water entering the heat exchanger (K)	433.6
Subcritical ORC Parameters	
The pressure of ORC working fluid entering the heat exchanger (kPa)	3000
The temperature of ORC working fluid entering the heat exchanger (K)	343.14
The temperature of ORC working fluid entering the turbine (K)	370
Supercritical ORC Parameters	
The pressure of ORC working fluid entering the liquid region zone of the heat exchanger (kPa)	4370
The temperature of ORC working fluid entering the liquid region zone of the heat exchanger (K)	360
The temperature of ORC working fluid leaving the supercritical region zone of the heat exchanger (K)	390

4.3 Results for Shell and Tube Heat Exchanger Integrating ORC and PTSC

In this section, the results of shell and tube heat exchanger integrating ORC and PTSC are presented in the following subsections. For this heat exchanger, the results are divided into two sections which are analytical modeling results and CFD modeling results.

4.3.1 Results for Analytical Modelling of Shell and Tube Heat Exchanger Integrating ORC and PTSC

4.3.1.1 Effect of Tube Diameter on the Performance of the Heat Exchanger

The effect of outer diameter of the tube on the performance of the system was assessed using the data given in Table 5. Different values for this diameter were taken from TEMA standards (Harrison, 2007). In TEMA standards, tube diameters have 10 values, which are 0.0064 m, 0.0095 m, 0.0127 m, 0.0157 m, 0.0191 m, 0.0222 m, 0.0254 m, 0.0318 m, 0.0381 m, and 0.0508 m. Using the code developed in EES, a parametric study was conducted for these values for the outer diameter of the tube. As a result of this study, the change of heat transfer surface area and pumping power with respect to this diameter was found. The parametric study was repeated for different number of passes (1, 2 and 3), layout angles (30°, 45°, 60°, and 90°), and the different baffle configurations (segmental, continuous and non-continuous) and the results for these studies are shown as follows.

Fig. 4.1 shows the change of heat transfer surface area and pumping power for different values of outer diameter of the tube and the number of passes. The results show that increasing the outer diameter of the tube, the heat transfer surface area and the pumping power both fluctuate as the difference between the tube pitch and the outer diameter of tube also fluctuate with this increase. In addition, it can be seen that taking this parameter as small as possible (0.0064 m), the heat transfer surface area gets its lowest value. The reason of this trend can be attributed to the change the flow regime. In addition, the effect of this parameter on the pumping power is more

significant when the outer diameter of the tube is less than 0.0222 m. When this diameter is 0.0127 m, the pumping power is at its maximum value. This finding can be explained as follows. As the outer diameter increases, the equivalent diameter increases and thus pumping power decreases. These figures also show that the number of passes does not have a significant effect on the results but it only changes the number of tubes required. Taking the number of passes as 1 yield slightly higher heat transfer surface area compared to a heat exchanger with 2 or 3 tube passes.

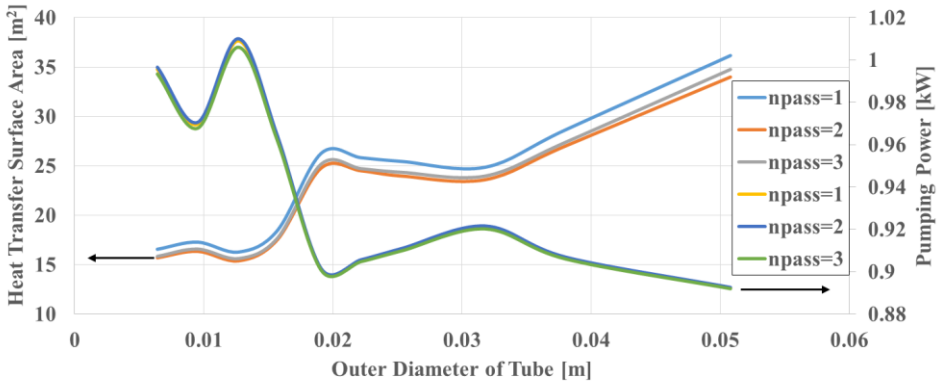

Figure 4.1 The effect outer diameter of tube on the heat transfer surface area and the pumping power for different number of passes

Figure 4.2 shows the change of heat transfer surface area and pumping power for different values of outer diameter of the tube and the tube layout angles. The results show that increasing the outer diameter of the tube, heat transfer surface area and pumping power fluctuate. If tube layout angle is selected 30° or 60° instead of 45° or 90°, heat transfer surface area decreases; whereas pumping power increases.

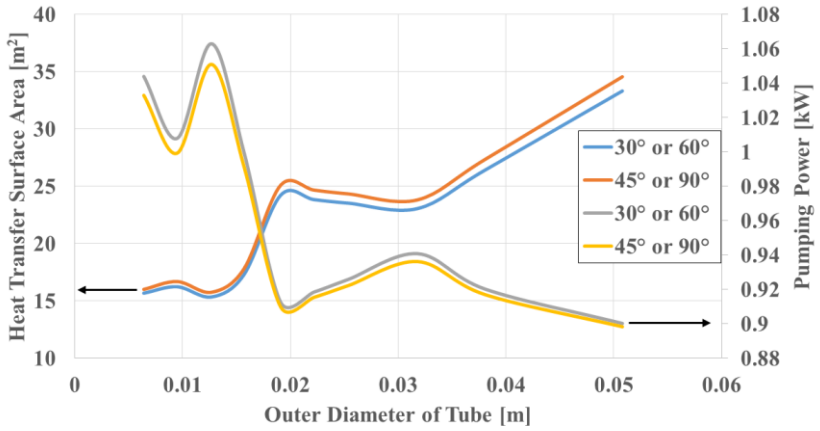

Figure 4.2 The effect outer diameter of tube on the heat transfer surface area and the pumping power for different tube layout angles

Figure 4.3 (a) shows the shell side heat transfer coefficient for different outer tube diameter and baffle configurations. The results from the figure show that increasing the outer tube diameter, shell side heat transfer coefficient fluctuates. This trend is mainly due to change in the flow regime. In addition, Figure 4.3 (a) illustrates that the shell side heat transfer coefficient of non-continuous baffles is higher than that of the segmental and continuous type baffles. Figure 4.3 (b) shows the change of total pressure drop of the system for different values of outer tube diameters, and the baffle configurations. The results show that increasing the outer tube diameter fluctuates the total pressure drop of the system. On the other hand, non-continuous baffle type causes higher pressure drop than that of the segmental baffle and continuous baffle types. Figure 4.3 (b) also shows that when the tube diameter is 0.0258 m, the total pressure with continuous baffle has the lowest value (32.79 kPa), and if tube diameter is 0.0508 m the total pressure drops of segmental and non-continuous baffles type heat exchangers are 36.52 kPa and 350.40 kPa, respectively.

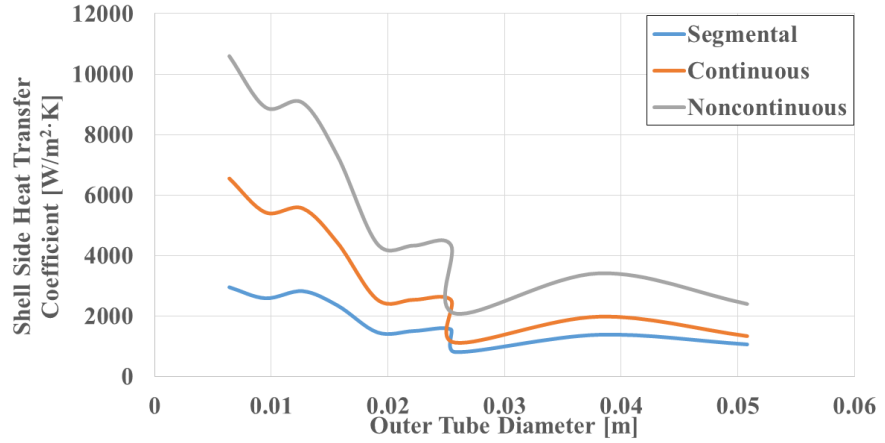

(a)

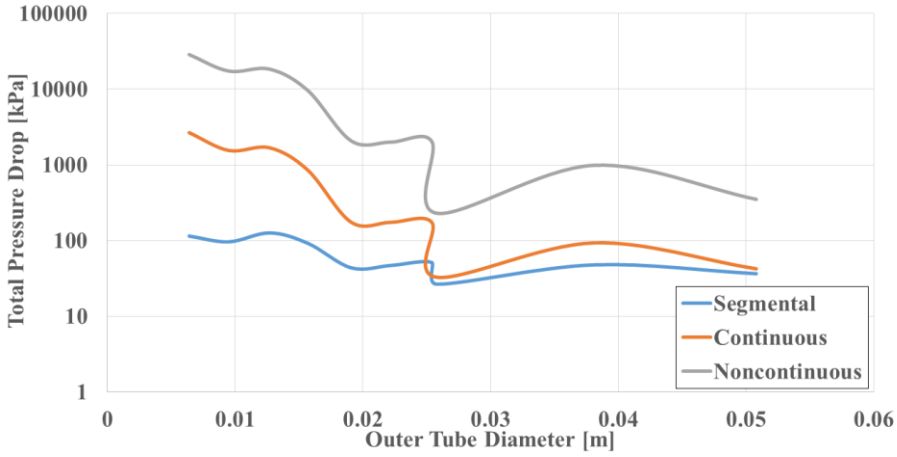

(b)

Figure 4.3 The effect of outer tube diameter on (a) shell side heat transfer coefficient, (b) total pressure of the system for different baffle configurations

Figure 4.4 (a) presents the change of the shell side heat transfer coefficient for the outer tube diameter and continuous baffle type of shell and tube heat exchanger according to different helix angles. It can be seen from this figure that the shell side heat transfer coefficient increases with a decrease in the helix angle. This variation trend can be understood from two aspects. First, at fixed shell diameter, the baffle spacing and the crossectional area of the shell perpendicular to the flow direction increase with an increase in the helix angle. Second, Reynolds number of the shell side fluid decreases with an increase in the helix angle. Thus, the convective heat transfer coefficient of the shell side increases. On the other hand, Figure 4.4 (b) shows the change of the total pressure drop of the system for the outer tube diameter and continuous baffle type heat exchanger according to different helix angles. The results

show that the pressure drop decreases with decreasing the helix angles. This trend is mainly due to the increase in the helix angle, hence the baffle spacing and crossectional area of the shell perpendicular to the flow direction increase with an increase in the helix angle, and the shell side mass velocity decreases thus the total pressure drop decreases.

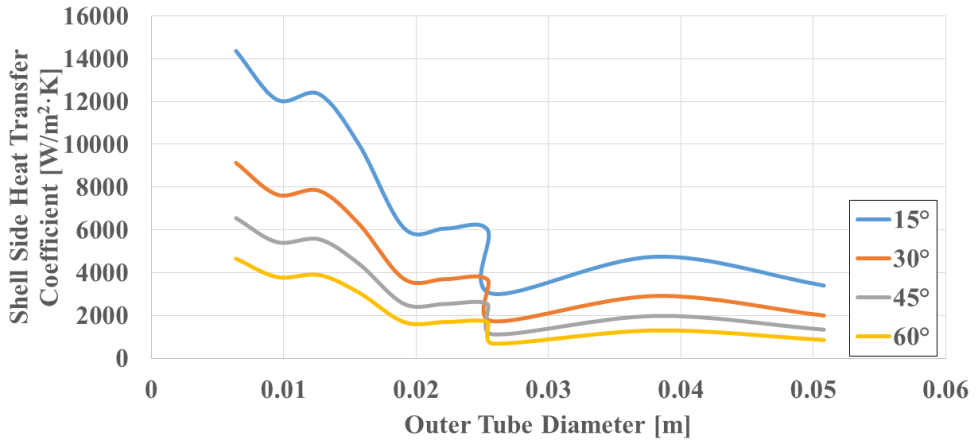

(a)

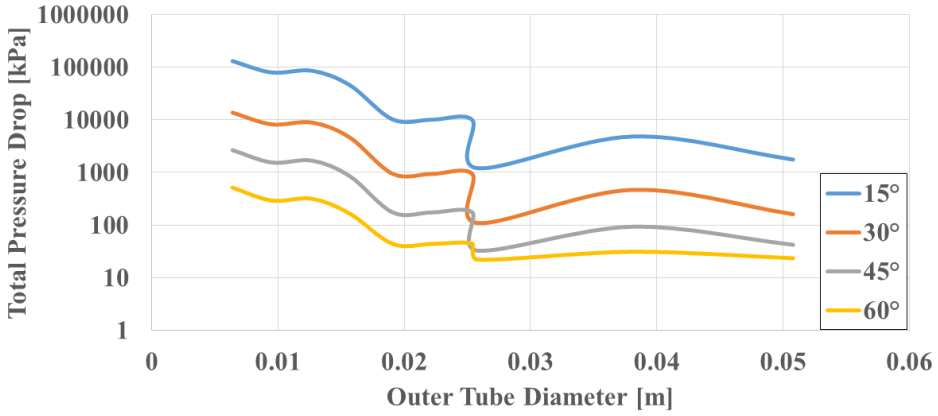

(b)

Figure 4.4 The effect of the outer tube diameter on the (a) shell side heat transfer coefficient, (b) total pressure drop for different helix angles with continuous helical baffle type

Figure 4.5 (a) illustrates the change of the shell side heat transfer coefficient for the different outer tube diameter and the non-continuous type baffle configurations. It can be seen from this figure that decreasing the helix angle increases the shell side heat transfer coefficient. On the other hand, Figure 4.5 (b) shows that the change of total

pressure drop for non-continuous heat exchanger and the outer tube diameter. The results show that an increase the helix angle decreases the total pressure drop.

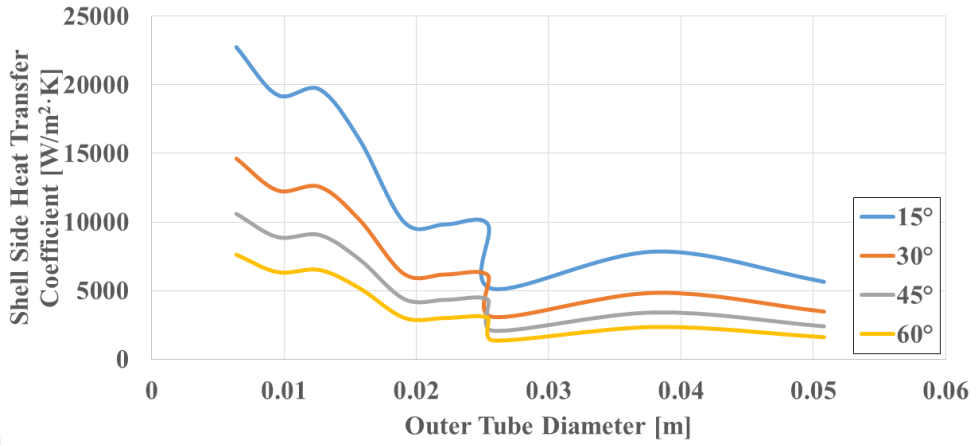

(a)

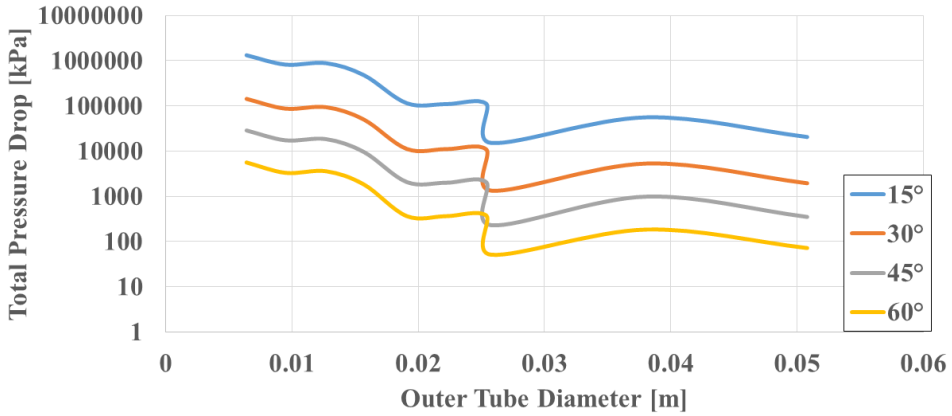

(b)

Figure 4.5 The effect of outer tube diameter on (a) Shell side heat transfer coefficient, (b) Total pressure drop for different helix angles with non-continuous baffle type

4.3.1.2 Effect of the Tube Length on the Performance of the Heat Exchanger

Ten different values of tube lengths can be found in TEMA standards. These values are 2.438 m, 3.048 m, 3.658 m, 4.877 m, 6.096 m, 7.32 m, 8.53 m, 9.75 m, 10.7 m, and 11.58 m (Harrison, 2007). Using the EES code, parametric studies were conducted for these values, and are presented and discussed below.

Figure 4.6 shows the change of the heat transfer surface area and pumping power for different values of tube length and number of passes. The results show that increasing the tube length, the heat transfer surface area decreases. This trend may be due to the change in the flow regime from laminar to turbulent when the tube length increases; and thus the tube side heat transfer coefficient increases however the number of tubes decreases. When the tube length is taken as high as possible (11.58 m), the overall heat transfer coefficient gets it maximum value, and the heat transfer surface area becomes minimum. On the other hand, it can be seen from Figure 4.6 that the pumping power changes between 0.88 kW and 0.94 kW; and the number of pass does not have a significant effect on these parameters.

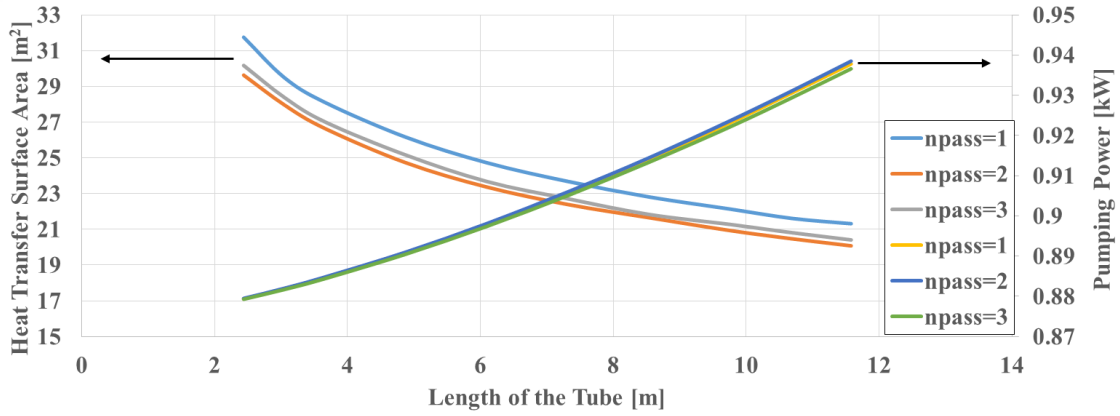

Figure 4.6 The effect of the tube length on the heat transfer surface area and the pumping power for different number of passes

Figure 4.7 shows the change of heat transfer surface area and pumping power for different values of tube length and layout angles. This figure presents that when the tube layout angle is 30° or 60°, the pumping power is higher; however heat transfer surface area is lower. Tube layout angle does not have a significant effect on the number of tubes. The tube layout angle depends on the tube layout constant. If the tube layout angle is 30° or 60°, the value of CL and shell diameter are lower than the values of those when the tube layout angle is 45° or 90°. Thus, the shell side fluid velocity, the overall heat transfer coefficient, the pressure drop and the pumping power slightly increase; whereas the heat transfer surface area slightly decreases.

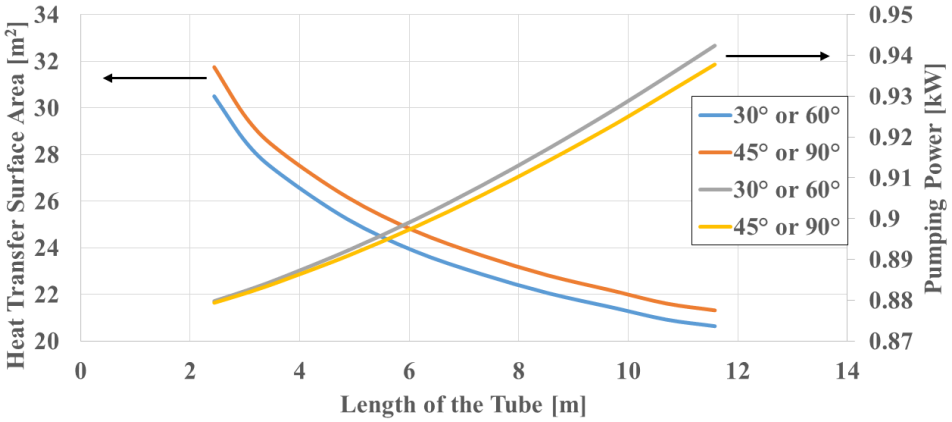

Figure 4.7 The effect of the tube length on the heat transfer surface area and the pumping power for different tube layout angles

Figure 4.8 (a) shows the change of the shell side heat transfer coefficient for the tube length and different baffle configurations. It can be seen from this figure, increasing the tube length increases the shell side heat transfer coefficient. Under the same helix angle, shell diameter, and tube length, the shell side heat transfer coefficient of the non-continuous baffle is around 71.7% higher than that of the continuous baffle type. This trend may be due to the increase in the tube length, thus the increase in the cross-sectional area of the shell perpendicular to flow direction, the increase in the Reynolds number of shell side, and the increase in the convective heat transfer coefficient of the shell side. However, when the tube length is 2.438 m, the shell side coefficient of the segmental baffle type is higher than that of the continuous type. Figure 4.8 (b) illustrates the change of the total pressure drop for the tube length and different baffle configurations. The results show that under the same tube length, the total pressure drop of the non-continuous baffle type heat exchanger is the highest among the other baffle types. This trend can be understood from following two aspects. First, the shell side mass velocity increases with an increase in the total pressure drop. Second, the shell diameter and helix angles are taken as constant in comparison. The baffle spacing of the continuous type heat exchanger is higher than that of the other types; whereas the shell side mass velocity decreases with a decrease in the total pressure drop. However, when the tube length is between the 2 m and 4 m, the total

pressure drop of the continuous type heat exchanger is lower than that of the segmental type heat exchanger.

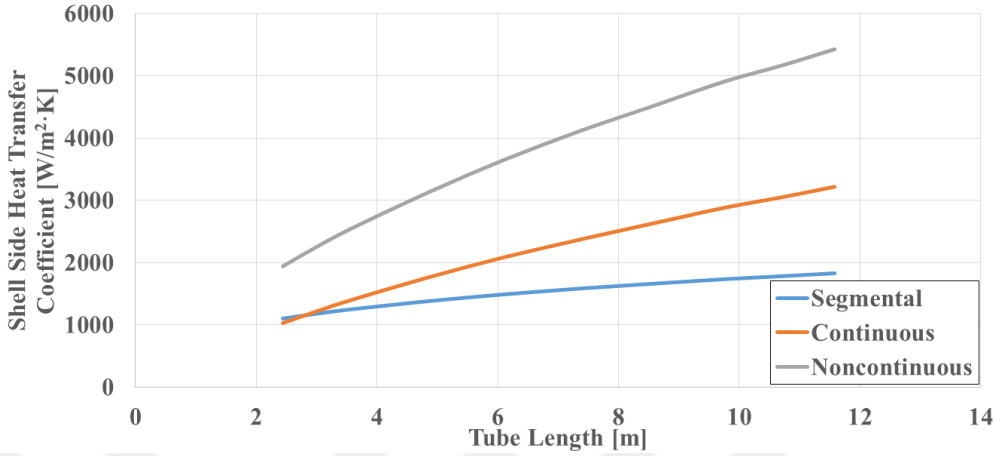

(a)

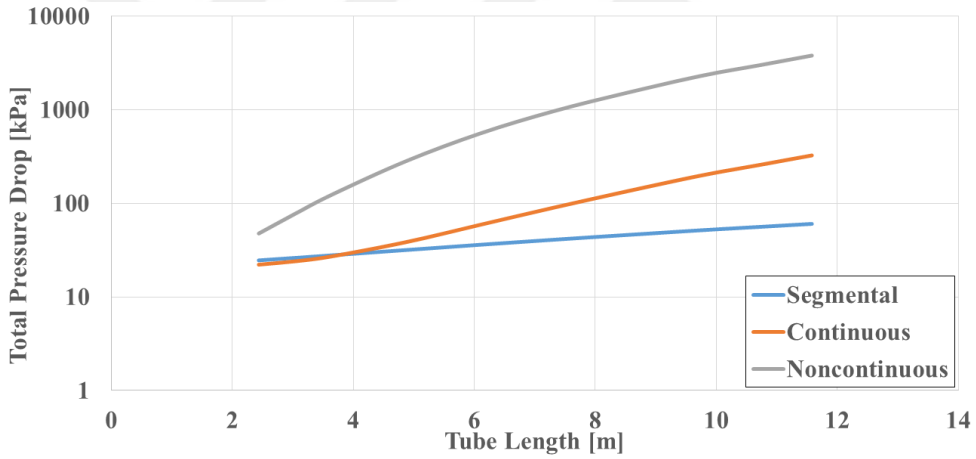

(b)

Figure 4.8 The effect of tube length on (a) shell side heat transfer coefficient, (b) total pressure drop of the system for different baffle configurations

Figure 4.9 (a) shows the change of shell side heat transfer coefficient for different tube length and helix angles for continuous baffle type. The results show that the shell side heat transfer coefficient increases with a decrease in the helix angle. This trend may be due to the decrease in the helix angle with a decrease in the baffle spacing. Thus shell side heat transfer coefficient increases. Figure 4.9 (b) illustrates the change of the total pressure drop of the system among three helical angles within the range of the tube length. The results show that the total pressure drop decreases with an increase

in the helix angles. As the helix angle increases, the baffle spacing increases, the crossectional area of the shell perpendicular to the flow direction increases, and the shell side mass velocity decreases. Thus, the total pressure drop of the system decreases.

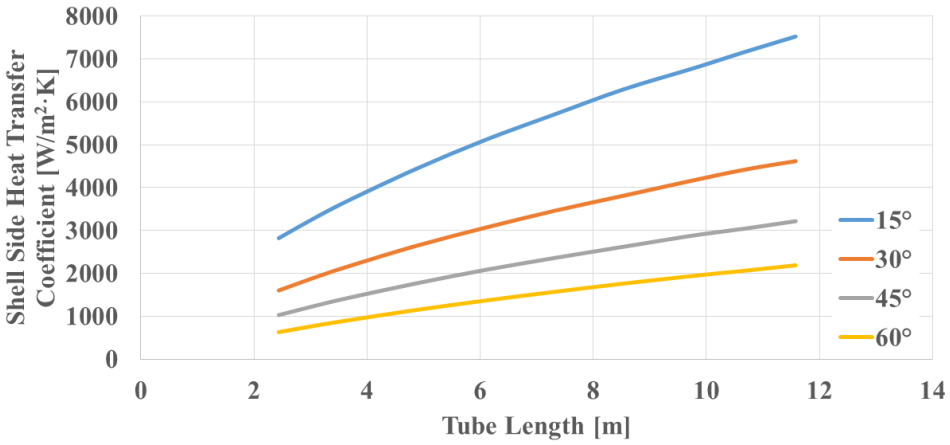

(a)

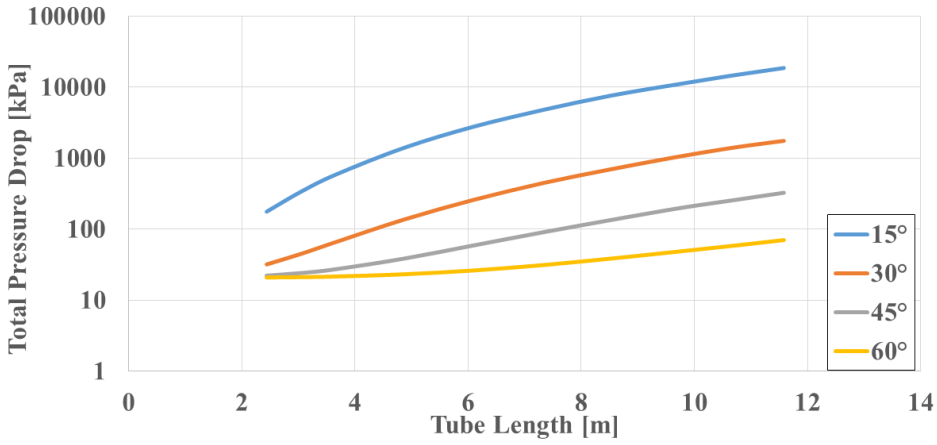

(b)

Figure 4.9 The effect of the tube length on (a) shell side heat transfer coefficient, (b) total pressure drop of the system for different helix angles with continuous type heat exchanger.

Figure 4.10 (a) illustrates the variation trends of shell side heat transfer coefficient with tube length for non-continuous baffle type heat exchanger. The results show that the shell side heat transfer coefficient increases with the decrease in the helix angles. On the other hand, Figure 4.10 (b) shows that the change of the total pressure drop of the system for the different tube length and helix angles for the non-continuous baffle

type heat exchanger. The results show that total pressure drop decreases with an increase in the helix angle.

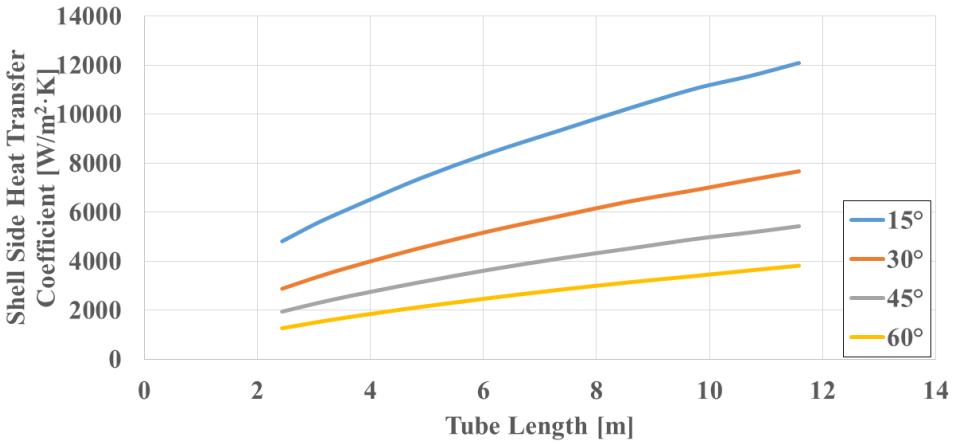

(a)

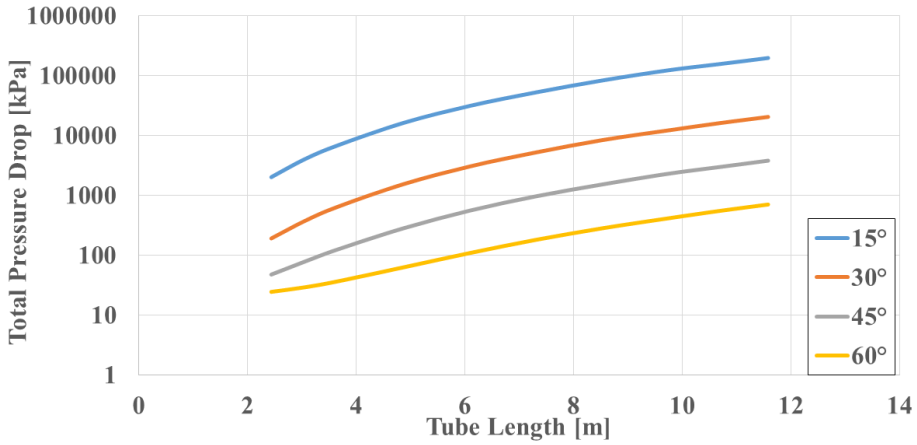

(b)

Figure 4.10 The effect of the tube length on (a) shell side heat transfer coefficient, (b) total pressure drop of the system for different helix angles with non-continuous type heat exchanger.

4.3.1.3 Effect of Baffle Spacing on the Performance of the Heat Exchanger

Minimum and maximum baffle spacing values are shown in Table 5. Minimum baffle spacing is found using the TEMA standards (Harrison, 2007); whereas the maximum baffle spacing can be found using Eq. (4.1) (Fettaka, Thibault, & Gupta, 2013).

$$e_{max} = 29.5{d_o}^{0.75} \tag{4.1}$$

Figure 4.11 shows the change of heat transfer surface area and pumping power for different values of baffle spacing and number of passes. The results show that increasing the baffle spacing increases the heat transfer surface area. This trend may be due to the fact that as the baffle spacing decreases, the effect of the turbulence and thus the shell side heat transfer coefficient decreases. When the baffle spacing is 0.08 m, the overall heat transfer coefficient is at its maximum value (1040 W/m^2·K) and the heat transfer surface area is at its minimum value (22.17 m^2). On the other hand, if the baffle spacing is 1.5 m, overall heat transfer coefficient takes its minimum value (115 W/ m^2·K) and the heat transfer surface area gets its maximum value (126.2 m^2). These results show that the baffle spacing should be selected as low as possible (0.08 m). The effect of number of passes on the results seems to be negligible. Figure 4.11 shows that increasing the baffle spacing first sharply decreases the pumping power up to the point where the baffle spacing is 0.32 m and then this parameter almost remains constant with a further increase in the baffle spacing. This result is mainly due to the change in the flow regime. When the baffle spacing increases from 0.08 m to 1.5 m, the Reynolds number decreases from 1422000 to 72189; hence the flow regime gets closer to laminar flow when the baffle spacing is increased.

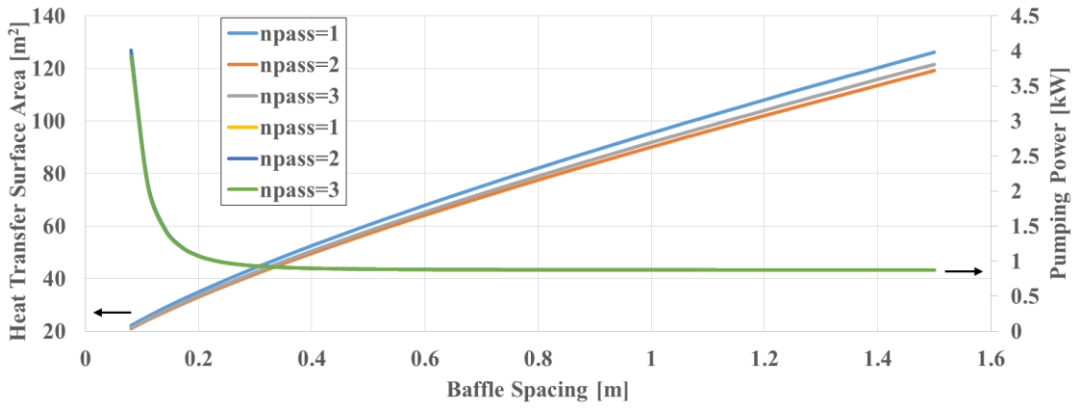

Figure 4.11 The effect of the baffle spacing on the heat transfer surface area and the pumping power for different number of passes

Figure 4.12 shows the change of the heat transfer surface area and the pumping power for different values of baffle spacing and tube layout angle. If the tube layout angle is 45° and 90° instead of 30° and 60°, the heat transfer surface area increases. It can also be seen from Figure 4.12 that the effect of tube layout angle on the pumping power is not significant.

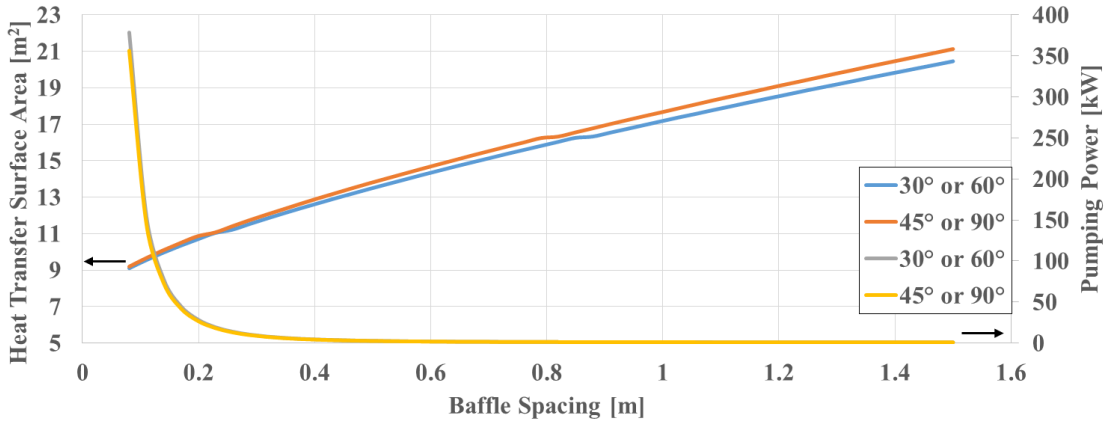

Figure 4.12 The effect of the baffle spacing on the heat transfer surface area and the pumping power for different tube layout angles

4.3.1.4 Effect of Solar Irradiation on the Performance of the Heat Exchanger

In this subsection, the effects of the solar irradiation intensity on the heat transfer surface area, the overall heat transfer coefficient, and the pumping power have been investigated. The selection of the solar irradiation intensity was done considering the minimum and maximum values of this parameter in the world. Countries such as Egypt, Sudan, Chad, Algeria in Africa and Chile in South America have maximum global irradiation; whereas locations such as Canada, Russia, Alaska, and Antarctica have minimum solar irradiation (Goswami & Besarati, 2013). In this study, global solar irradiation were taken between 450 W/m^2 to 1000 W/m^2.

The changes of heat transfer surface area, overall heat transfer coefficient, and pumping power with respect to solar irradiation intensity are presented in Fig. 4.13. Fig 4.13 (a) shows that overall heat transfer coefficient decreases with an increase in the solar irradiation. This may be due to the fact that increasing the solar irradiation,

outlet temperature of PTSC fluid and outlet temperature of the tube side fluid increase. Thus, the specific heat of the PTSC fluid increases; however density, viscosity, and Prandtl number of the PTSC fluid decreases. On the other hand, the viscosity of the tube side fluid increases, while specific heat, density, and Prandtl number of the tube side fluid decreases. Hence, Reynolds numbers of the both fluids decrease, which in turn decreases the shell side and tube side heat transfer coefficients. Due to these changes in these parameters, the overall heat transfer coefficient decreases. Fig. 4.13 (a) also presents that the heat transfer surface area increases (from 2.644 m^2 to 8.681 m^2) when the solar irradiation increases (from 450 W/m^2 to 1000 W/m^2) as the overall heat transfer coefficient and heat transfer surface area are inversely proportional. Fig. 4.13 (b) shows that pumping power increases from 0.8654 kW to 0.8771 kW when the solar irradiation increases from 450 W/m^2 to 1000 W/m^2. This increase is expected since, according to Eq. 3.29, the viscosity ratio between the bulk and wall temperatures (φ_{shell}) decreases with an increase in the solar irradiation and the temperature of the thermal oil leaving the PTSC. Thus, the pressure drop of the shell side of the heat exchanger increases. On the other hand, according to Eq. 3.58, the specific volume of the thermal oil circulating in the PTSC loop increases with an increase in both the solar irradiation and the temperature of the thermal oil leaving the PTSC.

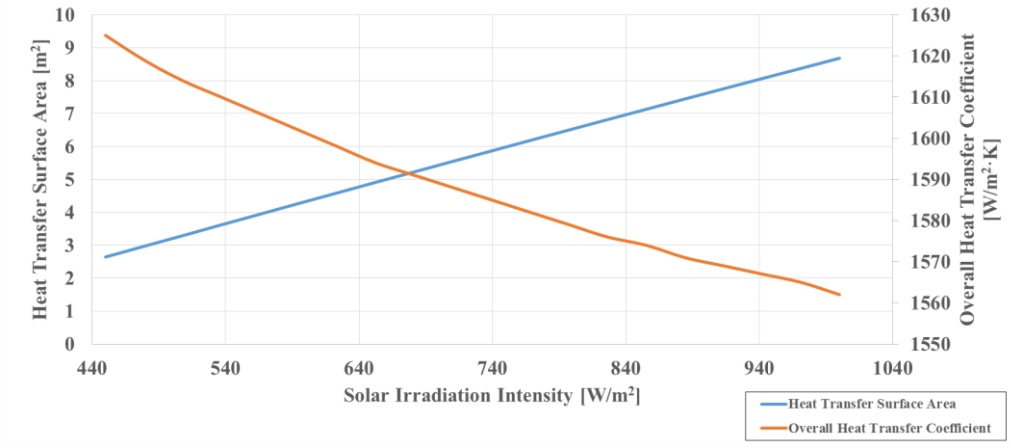

(a)

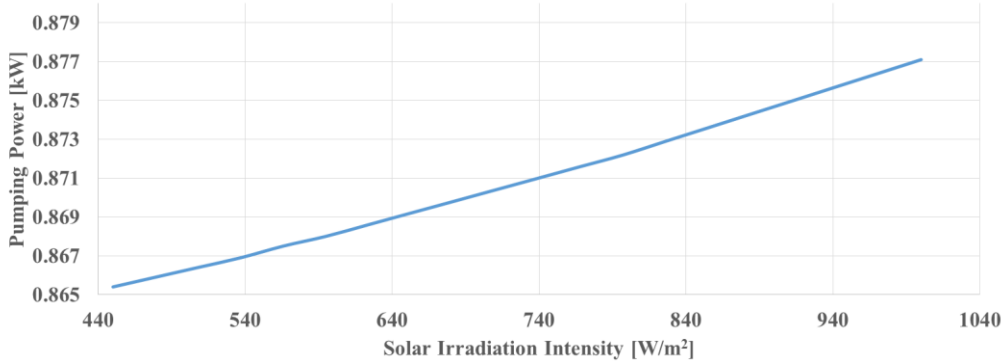

(b)

Figure 4.13 The effect of the solar irradiation intensity on (a) the optimum overall heat transfer coefficient and the heat transfer surface area, (b) pumping power

Figure 4.14 (a) shows the change of solar radiation with respect to shell side heat transfer coefficient according to different baffle configurations. The results show that increasing the solar radiation decreases the shell side heat transfer coefficient. This trend is mainly due to the fact that if the solar radiation increases, the outlet temperature of the PTSC fluid increases, the thermo-physical properties of the fluid such as viscosity, density, and conductivity increases. Hence, the shell side heat transfer coefficient decreases. On the other hand, under the same solar irradiation, the shell side heat transfer coefficient of the non-continuous type baffle is higher than the other baffle types of the shell and tube heat exchanger. Figure 4.14 (b) shows that the effect of the solar radiation on the total pressure drop of the system according to the different baffle types. This figure shows that when the non-continuous baffle is used, the total pressure drop is the highest. On the other hand, increasing the solar radiation

decreases the total pressure drop. As the solar radiation increases, the outlet temperature of the PTSC side fluid increases, thus the density of PTSC fluid and the rate of viscosities (φ_{shell}) increase. Thus, the total pressure drop decreases. In addition, when the solar radiation is approximately 970 W/m^2, the total pressure drop of the segmental and continuous baffle types are close to each other.

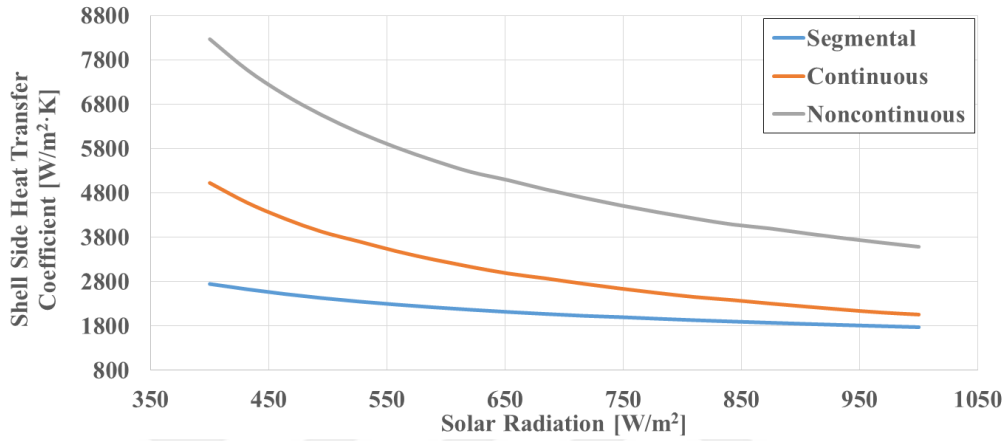

(a)

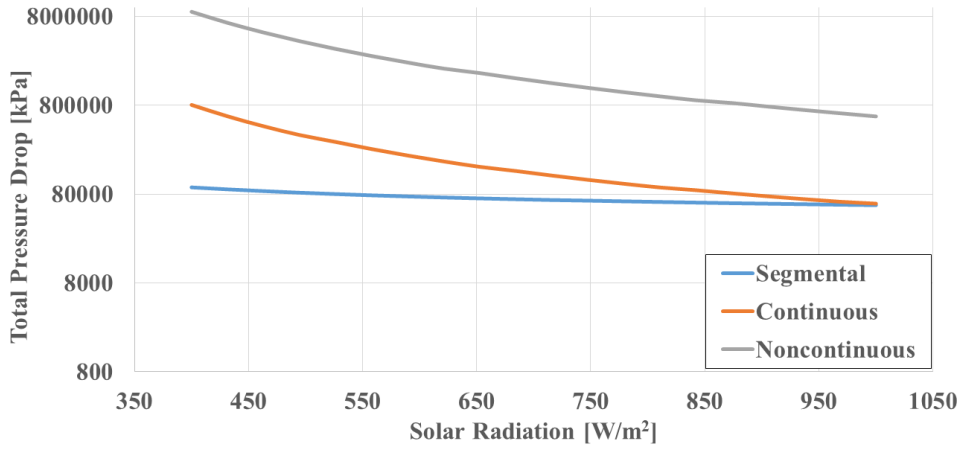

(b)

Figure 4.14 The effect of solar radiation on (a) shell side heat transfer coefficient, (b) total pressure drop of the system for different baffle configurations

4.3.1.5 Effect of Organic Rankine Cycle Working Fluid Type on the Performance of the Heat Exchanger

The importance of the fluid selection and their properties is discussed and emphasized in Section 2.4. In this section the effect of organic Rankine cycle working

fluid on the performance of the heat exchanger is discussed. Figure 4.15 shows the effect of ORC side fluid type on the heat transfer surface area and pumping power. This figure shows that the heat exchanger operating with R245fa has smaller heat transfer surface area than that with other working fluids. This finding is related to the differences in the thermo-physical properties of these fluids. Density, viscosity, and Prandtl are the highest, and conductivity and specific heat are the lowest for R245fa, it has the highest overall heat transfer coefficient. However, as R245fa has high global warming potential (GWP) value (1030) than R600 (GWP of 4) (Linde Gas, 2015), R600 should be selected as the fluid type considering both energetic and environmental effects. Figure 4.15 shows that R502 has the smallest pumping power among the fluid types studied. The ratio of density to dynamic viscosity (or Reynolds number) is higher for R502; hence the friction factor and the pressure drop are lower for this fluid type.

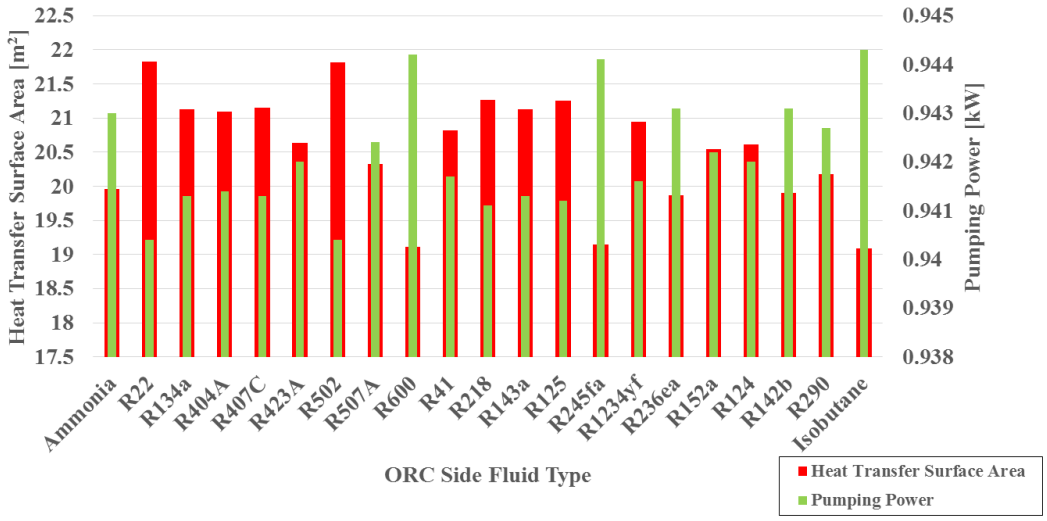

Figure 4.15 The effect of the different ORC side working fluid on the heat transfer surface area and the pumping power

4.3.2 Results for CFD Modelling

Beginning with the velocity variation within the shell and tube heat exchanger shown in Figure 4.16, it can be seen that the velocity and velocity variations of the shell-side fluid increased linearly with increasing inlet mass flow rates. For instance, the standard deviation in the velocity variations in each case was: 3.7 m/s, 7.4 m/s, and 13 m/s, for the 28 kg/s, 55 kg/s and 138 kg/s cases, respectively. These velocity

variations primarily occurred due to the shell-side fluid passing across the baffles within the shell. However, the detailed explanation of the observed fluctuations in the velocity field can be explained as follows. As the bulk flow approaches a baffle, the velocity begins to sharply increase due to the smaller cross-sectional area. Directly after this baffle, the cross-sectional area for the flow decreases causing a sharp decrease in velocity. Due to the sharp differences in the fluid's shear stress distribution, from above to behind the baffle, this causes a recirculation zone to appear. This recirculation can be seen by the "low velocity pocket" (the blue-colored zone behind each of the baffles in Figure 4.17). This recirculation causes fluctuations to occur within the bulk flow. However, as this recirculation zone is entrained into the bulk flow, the linear velocity of the bulk flow begins to decrease. At this point, the fluid is near the next baffle, and the process repeats. There also a few important features of the flow that should be noted. For instance, as the flow crosses a baffle, the velocity at the baffle, especially near the baffle-wall interface on both sides of the baffle, the velocity will stagnate. This will cause poor mixing, causing the flow to have a non-uniform temperature distribution. As such, HX designs should be careful to avoid such flow conditions. One possible route would be the inclusion of helical baffles as examined in Jayakumar et al., (2008); Lei et al., (2008); Taher et al., (2012); Zhang, He, & Tao, (2009).

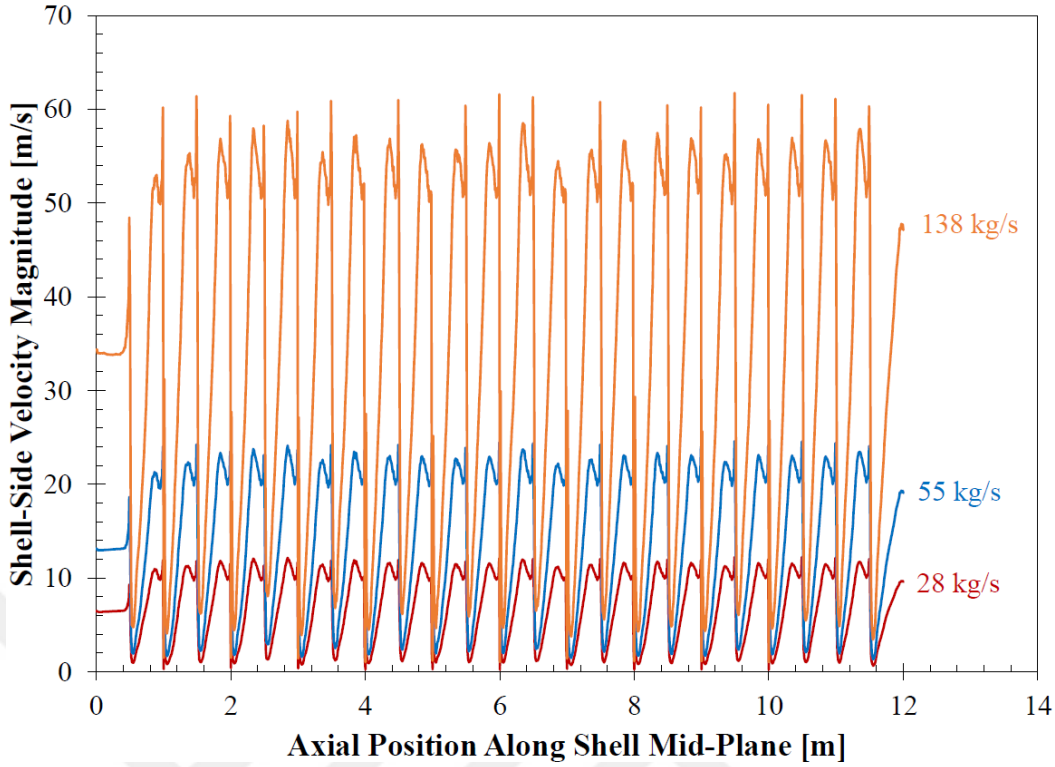

Figure 4.16 The velocity magnitude variation of the shell-side fluid, for different inlet shell-side mass flow rates, with respect to the axial position along the mid-plane of the heat exchanger

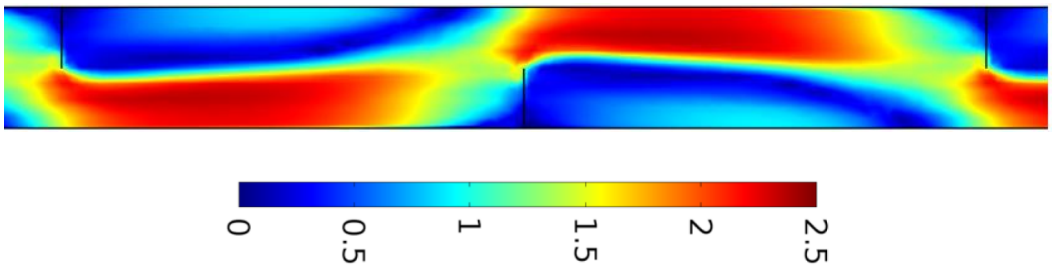

Figure 4.17 The normalized velocity distribution ($|u|/u_{inlet}$) within the shell, along the mid-plane. The axial position under consideration is from 2.5 m to 3.5 m along the shell

From this velocity distribution, the STHX's temperature distribution will be better understood. The temperature distribution of the shell-side fluid along the length of the shell and tube heat exchanger is shown in Figure 4.18. As can be seen, as the flow rate is increased, the temperature difference, ΔT, across the shell-side fluid decreases (ΔT = 133°C, 114°C and 78.0°C, for the 28 kg/s, 55 kg/s and 138 kg/s cases, respectively). There are also temperature fluctuations along the shell's length (~10°C each) due to

the conductive thermal resistance imposed by the baffles. Furthermore, the re-circulation zones behind each of the baffles, as shown in Figure 4.17 and discussed in the previous paragraph, shrink as the bulk fluid travels along the length of the STHX because of the entrainment of the lower velocity recirculated fluid. This allows the colder recirculated fluid to mix with the hot bulk fluid. This causes the average fluid temperature to increase. This distribution can be seen in the temperature contour plot in Figure 4.18.

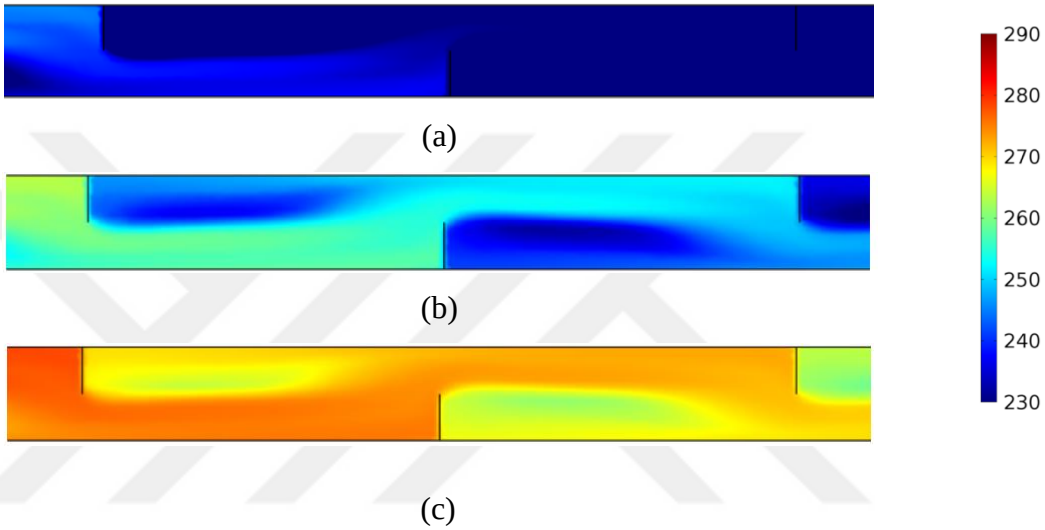

Figure 4.18 The temperature distribution, in [°C], within the shell, along the mid-plane for an axial position from 2.5 m to 3.5 m along the shell. The subfigures (a)-(c) refer to the inlet mass flow rate cases of (a) 28 kg/s, (b) 55 kg/s and (c) 138 kg/s

4.4 Results for Shell and Tube Heat Exchanger Used for Integrating ORC and Geothermal Source

In this section, the results for shell and tube heat exchanger integrating ORC and geothermal source are presented in the following subsections. In this heat exchanger modeling, the heat exchanger was divided into several zones and the outlet conditions of each zone were calculated applying logarithmic mean temperature difference (LMTD) method. Different Nusselt correlations which are explained in Section 3.1, according to the relevant phase (single, two-phase and supercritical) were also used in this model. The results are presented following subsections.

4.4.1 Effect of the Tube Diameter on the Performance of the Heat Exchanger

Figures 4.19 (a) and 4.19 (b) show the change of tube side drop of subcritical ORC heat exchanger for each zone with respect to different inner diameter of tube. Figure 4.19 (a) shows that the tube side pressure drops of liquid and two phase zones decrease with an increase in the inner tube diameter. This trend can be explained as follows. When the inner diameter of tube increases, the velocity of fluid in the liquid and two phase region zones decreases as well as the length of these zones. On the other hand, Figure 4.19 (b) shows that the inner diameter of tube increases with a decrease in the tube side pressure drop of vapor region zone. According to Figures 4.19 (a) and 4.19 (b), for the same tube diameter, the pressure drop in the two-phase region zone has the lowest value.

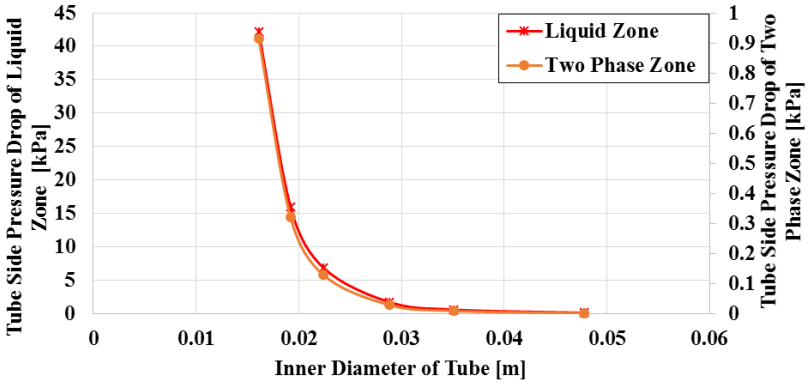

(a)

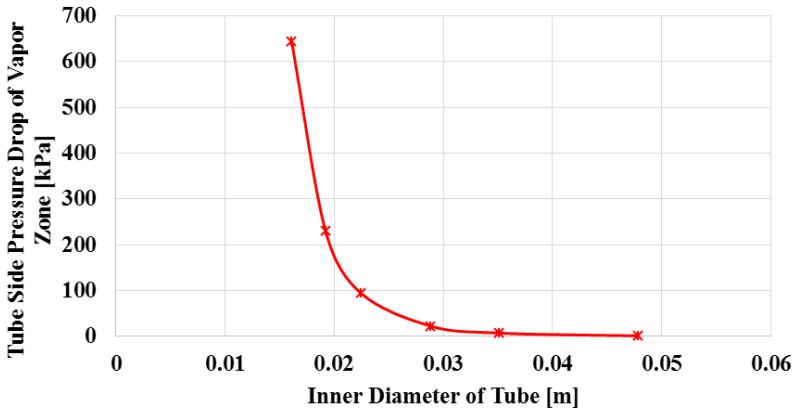

(b)

Figure 4.19 The effect of the inner diameter of tube on the (a) tube side pressure drop of the liquid and two phase zones, and (b) tube side pressure drop of the vapor zone

Figure 4.20 shows the change of tube side pressure drop of supercritical ORC heat exchanger for different values of inner diameter of tube. The tube side pressure drop of both zones sharply decreases with an increase in the inner diameter of tube. This trend is mainly due to the decrease in the velocity of tube side fluid for liquid and supercritical zones and decrease in the length of the liquid and supercritical zones. In addition, under the same inner diameter of tube, it is found that the tube side pressure drop of supercritical region zone is lower than that of the liquid zone tube side pressure drop.

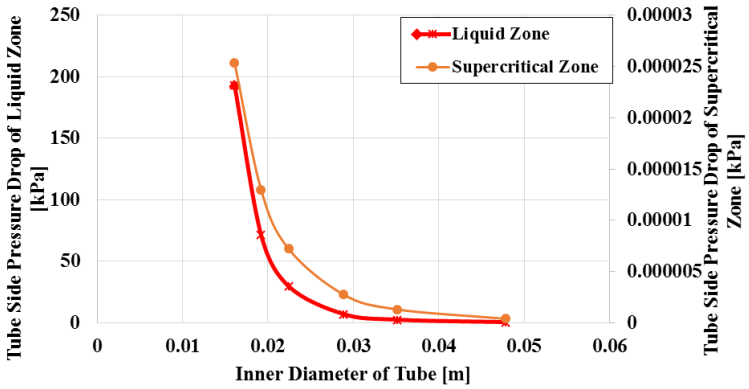

Figure 4.20 The effect of the inner diameter of tube on the tube side pressure drop of the liquid and supercritical zones

Figure 4.21 (a) shows the change of overall heat transfer of liquid, two phase and vapor zones for different values of inner diameter of tube. It can be seen from this figure increasing the inner diameter of tube, the overall heat transfer coefficient of liquid and vapor zones decreases. However, the overall heat transfer coefficient in the two-phase zone first increases until the inner tube diameter is 0.0351 m, then it starts to decrease. This reason may be due to change in the flow characteristics. The flow that can be identified as convection boiling flow gets closer to nucleate boiling flow. In addition, under the same inner diameter of tube, the overall heat transfer coefficient of the two phase zone has the highest value. On the other hand, Figure 4.21 (b) shows the change of overall heat transfer coefficient for supercritical ORC heat exchanger with respect to inner diameter of tube for two different zones which are liquid and supercritical zones. The results show that increasing the inner diameter of tube, the

overall heat transfer coefficient in the liquid and supercritical regions decreases. This trend may be due to the fact that as the inner diameter of tube increases, the Reynolds number of tube side fluid for liquid and supercritical zones decreases. Hence, Nusselt number of tube side fluid for both zones decreases as well as tube side heat transfer coefficient for liquid and supercritical zones. In addition, under the same inner tube diameter the overall heat transfer coefficient of supercritical region is higher than that of the overall heat transfer coefficient of the liquid region.

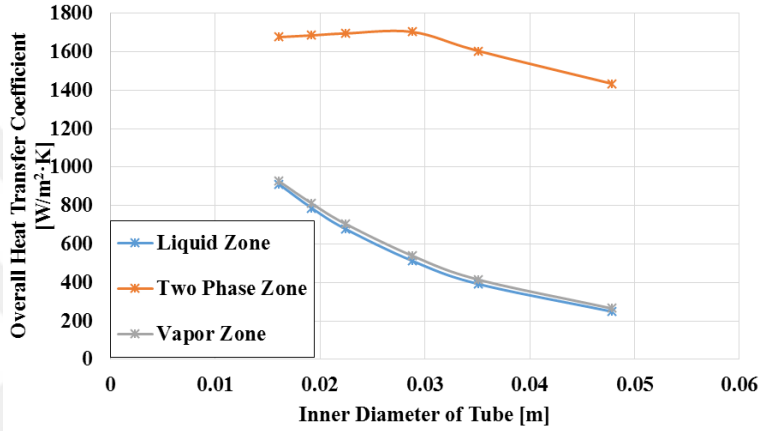

(a)

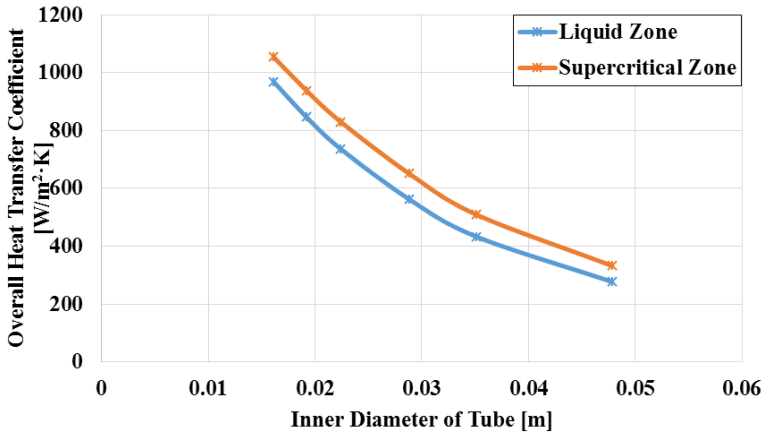

(b)

Figure 4.21 The effect of the inner diameter of tube on the (a) overall heat transfer coefficient of the liquid, two phase, and vapor zones, (b) overall heat transfer coefficient of the liquid and supercritical zones

The change of zone length for liquid region, two-phase region, and vapor region with the inner diameter of tube is given in Figure 4.22 (a). The results show that as the

inner diameter of tube increases, the length of liquid and supercritical zones decrease. It was found that when the inner diameter of tube is 0.0478 m, the length of liquid, two phase and vapor zones are calculated as 0.64 m, 3.08 m, and 2.19 m, respectively, and get their minimum values. In addition, under the same inner diameter of tube, zone length of two phase region gets the highest value among the other regions. Figure 4.22 (b) shows the change of zone length in liquid and supercritical regions with respect to inner diameter of tube. The results show that the length of each zone decreases with an increase in the inner diameter of tube. Under the same inner diameter of tube, it is found that the length of supercritical region is higher than the length of the liquid region.

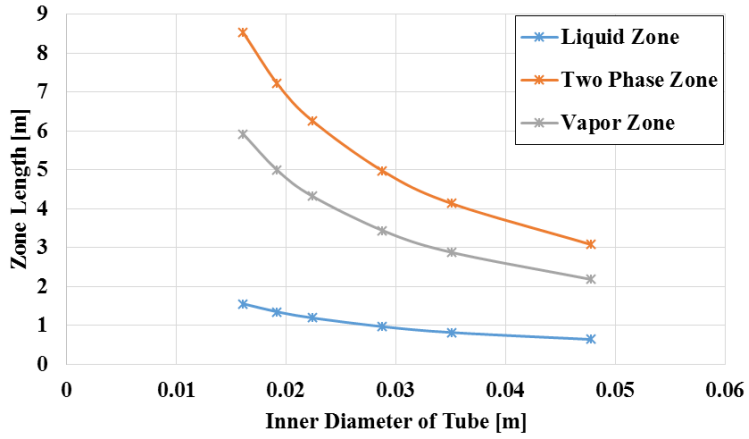

(a)

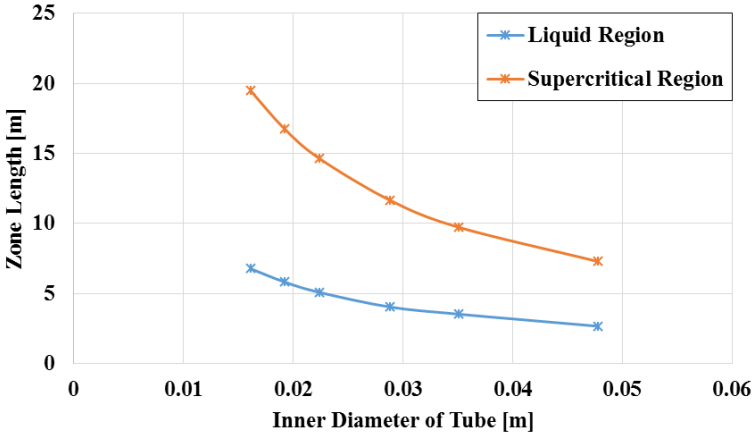

(b)

Figure 4.22 The effect of the inner diameter of tube on the (a) zone length of the liquid, two phase, and vapor zones, (b) zone length of the liquid and supercritical zones

4.4.2 Effect of Source Temperature on the Performance of the Heat Exchanger

In this subsection, the effect of source temperature on the performance of the heat exchanger according to different heat exchanger design configurations (e.g. single zone, and multi zone modelling), and different ORC working fluids was presented and discussed. The performance parameters are the heat transfer surface area, the pressure drop of tube side fluid. The results were given comparatively according to heat exchanger design configurations, and the type of working fluids. In this study, three different ORC working fluids which are R134a, R1234yf, and R1234ze(E) were selected. The fluid selection was done considering the most commonly used found from the open literature, and also new generation environmentally friendly fluids.

Figures 4.23 (a) and 4.23 (b) show the change of heat transfer surface area and tube side pressure drop for different values of source temperature and different design configurations of heat exchanger according to different ORC working fluids in subcritical ORC. As the source temperature increases, the heat transfer surface area and the tube side pressure drop decreases for different heat exchanger design configurations according to different ORC working fluid. This trend mainly due to the fact that when the source temperature increases, the shell side heat transfer coefficient increases as well as the overall heat transfer coefficient. Thus the heat transfer surface area decreases. On the other hand, when the source temperature increases, the tube side pressure drop decreases. This trend due to decrease in the zone length. In addition, under the same source temperature the heat transfer surface area and the pressure drop of tube side fluid of the zone modeling heat exchanger is higher than that of the single zone modeling of heat exchanger.

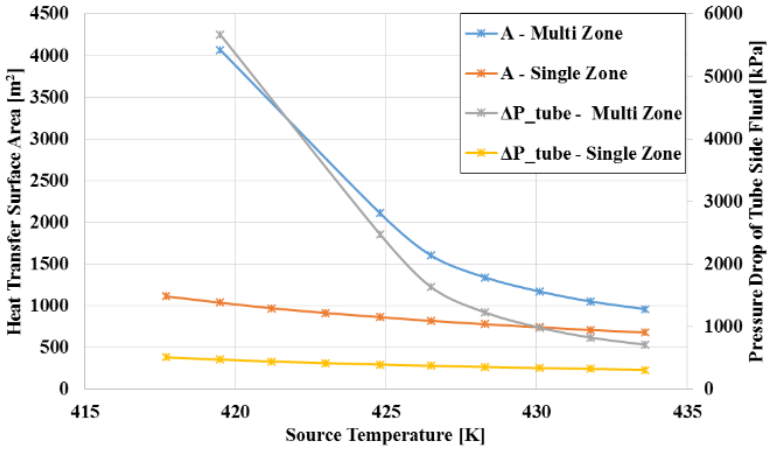

(a)

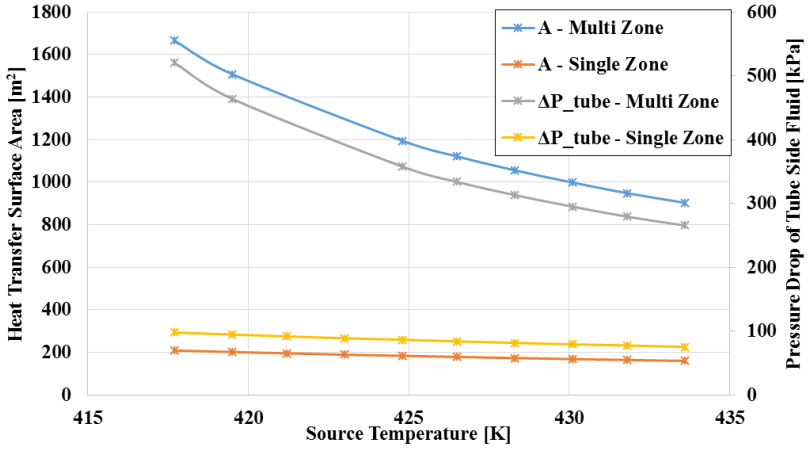

(b)

Figure 4.23 The effect of the source temperature on the (a) heat transfer surface area and pressure drop of tube side fluid for R134a, (b) heat transfer surface area and pressure drop of tube side fluid for R1234ze(E) in subcritical ORC

Figures 4.24 (a), (b), and (c) show the change of heat transfer surface area, and tube side pressure drop for the range of source temperatures and different heat exchanger configurations according to different ORC working fluids in supercritical ORC. In Figure 4.24 (a) when the source temperature increases, the tube side pressure drop of both single zone and multi zone modeling, and the heat transfer surface area of single zone modeling decrease. However the heat transfer surface area of multi zone modeling first decreases until when the source temperature is 417.7 K, after that increases. This trend due to the fact that as the source temperature increases with the increase in the length of the supercritical state of the heat exchanger. Hence the heat transfer surface area of multi zone modeling increase. On the other hand, in Figures

4.24 (b) and 4.24 (c) increasing the source temperature, the heat transfer surface area and the tube side pressure drop decreases. In addition, it can be seen from these figures when the R134ze(E) is used as working fluid, it was observed that the pressure drop, and the heat transfer surface area characteristics steadily decrease.

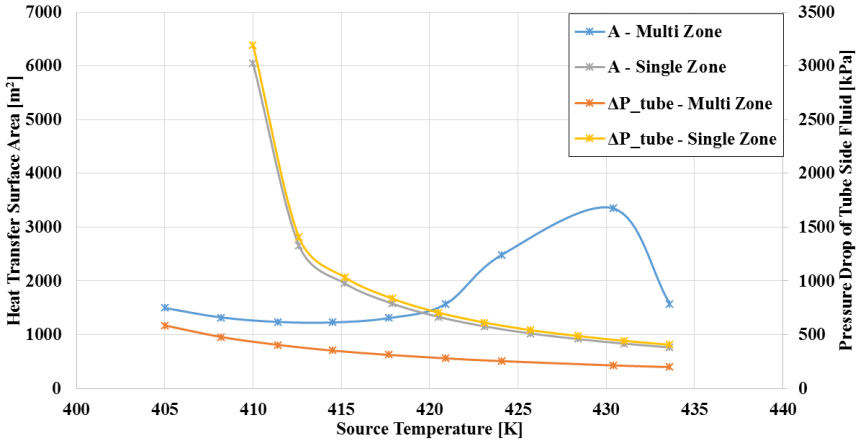

(a)

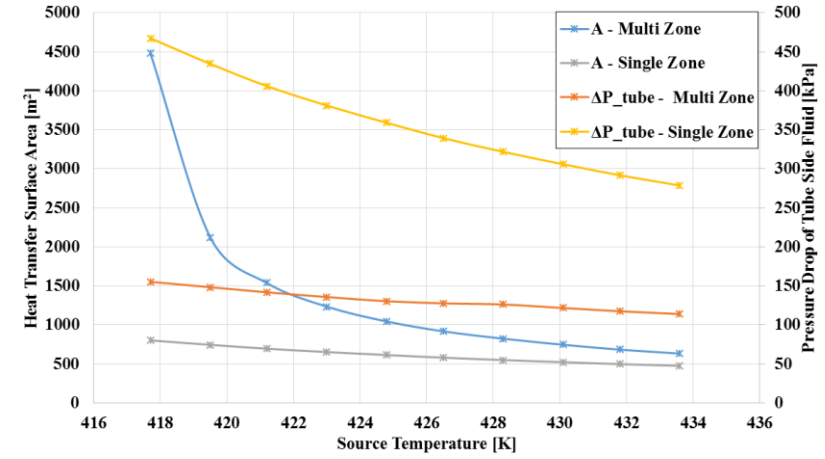

(b)

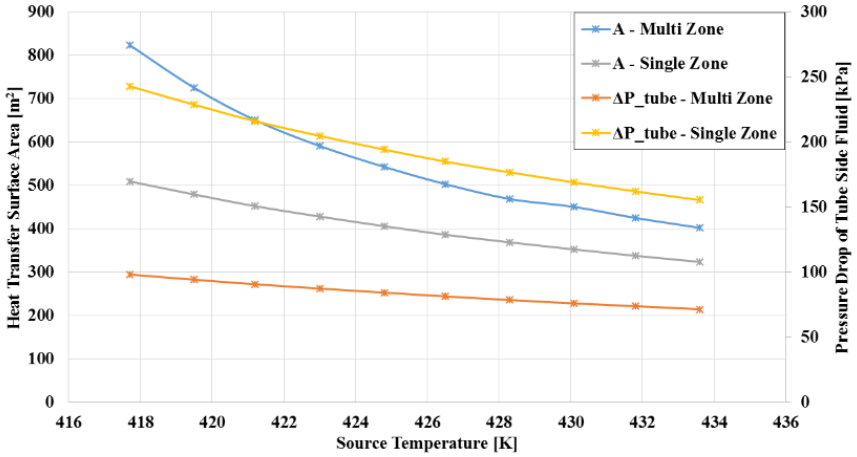

(c)

Figure 4.24 The effect of the source temperature on the (a) heat transfer surface area and pressure drop of tube side fluid for R134a, (b) heat transfer surface area and pressure drop of tube side fluid for R1234yf and (c) heat transfer surface area and pressure drop of tube side fluid for R1234ze(E) in supercritical ORC

CHAPTER FIVE
CONCLUSIONS

In this thesis, the design and analysis of a shell and tube heat exchanger, which combines a PTSC and an ORC, was done by applying the principles of thermal sciences. For this purpose, thermal models of the PTSC and the heat exchanger were first developed and then solved using 'Engineering Equation Solver' for a case study. Parametric studies were conducted to find the effect of some of the key design parameters on the output parameters of the model such as heat exchanger surface area and the pumping power. In addition a detailed thermal and mathematical model of shell and tube heat exchanger integrating ORC and geothermal source is formed. This heat exchanger was divided into three zones and two zones for subcritical and supercritical ORCs, respectively, and the outlet conditions of each zones were found using energy balance equations and the logarithmic mean temperature difference method. A parametric study was conducted to assess the effect of some important design and operating parameters (e.g. inner diameter of tube, the ORC source temperature) on the performance of the heat exchanger. The performance parameters are the overall heat transfer coefficient, the tube side pressure drop. The thermal model of the heat exchangers was developed using 'Engineering Equations Solver (EES)' software. The following main conclusions are derived as a result of these studies conducted in this thesis:

- When the tube length increases, the heat transfer surface area decreases; but the pumping power increases.
- If baffle spacing decreases, Reynolds number of shell side increases and the flow regime might become turbulent. Thus, the overall heat transfer coefficient increases as the spacing decreases. If baffle spacing increases from 0.08 m to 1.5 m, the overall heat transfer coefficient decreases from 1040 $W/m^2 \cdot K$ to 115 $W/m^2 \cdot K$.
- The parametric studies showed that if tube layout angle is chosen 30° or 60° instead of 45° or 90°, the heat transfer surface decreases and pumping power increases.

- The number of passes does not have a significant effect on the heat transfer surface area and the pumping power.
- When the solar irradiation increases from 450 W/m^2 to 1000 W/m^2, the minimum pumping power and heat transfer surface area increase from 0.8654 kW to 0.8771 kW and 2.644 m^2 to 8.681 m^2, respectively.
- The parametric studies showed that using R245fa as the ORC fluid give better performance. However, it is suggested that R600, which gives the second best performance as the ORC fluid should be used as it is less harmful to the environment.
- Helix angle has significant effect on the performance of the shell and tube heat exchanger. It is found that 15° helix angle possesses the best performance among the different types studied.
- Non-continuous baffle type heat exchangers should be preferred since the shell side heat transfer coefficient is the highest than the others. However, it is difficult to manufacture this type of heat exchanger. Thus, continuous baffle type heat exchanger may be preferred.
- It was found that when the inner tube diameter increases, the tube side pressure drop of liquid, two-phase, and vapor regions decreases in the subcritical ORC. On the other hand, the inner tube diameter increases with a decrease in the tube side pressure drop of liquid and supercritical regions in the supercritical ORC.
- It was observed that the inner diameter of tube increases with a decrease in the overall heat transfer coefficient of the liquid, two-phase, and vapor regions in the subcritical ORC. In addition, under the same inner diameter of tube it was found that the overall heat transfer coefficient of two-phase region is higher than the liquid and vapor regions in the subcritical ORC; whereas the overall heat transfer coefficient of supercritical region has the highest value among the other regions.
- It was found that, as the source temperature increases, the heat transfer surface area, and the pressure drop decreases for different heat transfer fluids.

REFERENCES

Al-Sulaiman, F. A. (2014). Exergy analysis of parabolic trough solar collectors integrated with combined steam and organic Rankine cycles. *Energy Conversion and Management*, *77*, 441-449.

ASHRAE (2008) Standard 34: Designation and Safety Classification of Refrigerants. ANSI Atlanta: ASHRAE.

Bhutta, M. M. A., Hayat, N., Bashir, M. H., Khan, A. R., Ahmad, K. N., & Khan, S. (2012). CFD applications in various heat exchangers design: A review. *Applied Thermal Engineering*, *32*, 1-12.

Biomass. (2016). Retrieved June 4, 2017 from https://en.wikipedia.org/wiki/Biomass

Cakici, D. M., Erdogan, A., & Colpan, C. O. (2017). Thermodynamic performance assessment of an integrated geothermal powered supercritical regenerative organic Rankine cycle and parabolic trough solar collectors. *Energy*, *120*, 306-319.

COMSOL User's Guide. (2015).

Goswami, D. Y. & Besarati, S.M. (2013). Retrieved May 16, 2017, from http://www.worldenergy.org/wpcontent/uploads/2013/10/WER_2013_8_Solar_revised.pdf.

DiPippo, R. (2012). *Geothermal power plants: principles, applications, case studies and environmental impact*. UK: Butterworth-Heinemann.

Dong, B., Xu, G., Luo, X., Zhuang, L., & Quan, Y. (2017). Analysis of the supercritical organic Rankine cycle and the radial turbine design for high temperature applications. *Applied Thermal Engineering*, DOI:10.1016/j.applthermaleng.2016.12.123.

Duffie, J. A., & Beckman, W. A. (1980). *Solar engineering of thermal processes*. USA: Wiley.

Enerji Enstitüsü. (2011). *Zorlu Denizli'de Türkiye'nin En Büyük Jeotermal Santralini Kuruyor*: Retrieved June 4, 2017, from http://enerjienstitusu.com/2011/12/14/zorlu-denizlide-turkiyenin-en-buyuk-jeotermal-santralini-kuruyor.

Erdogan, A., Colpan, C. O., & Cakici, D. M. (2017). Thermal design and analysis of a shell and tube heat exchanger integrating a geothermal based organic Rankine cycle and parabolic trough solar collectors. *Renewable Energy, 109*, 372-391.

Fang, X., Xu, Y., Su, X., & Shi, R. (2012). Pressure drop and friction factor correlations of supercritical flow. *Nuclear Engineering and Design, 242*, 323-330.

Fernandez-Garcia, A., Zarza, E., Valenzuela, L., & Pérez, M. (2010). Parabolic-trough solar collectors and their applications. *Renewable and Sustainable Energy Reviews, 14*(7), 1695-1721.

Fettaka, S., Thibault, J., & Gupta, Y. (2013). Design of shell-and-tube heat exchangers using multiobjective optimization. *International Journal of Heat and Mass Transfer, 60*, 343-354.

GWEC. (2012). *Global Wind Report: Annual Market Update 2012*. Retrieved June 16, 2017 from https://www.gwec.net/wpcontent/uploads/2012/06/Annual_report_2012_LowRes.pdf

Harrison, J. (2007). *Standards of the tubular exchangers manufacturers association*. New York: Tubular Exchangers Manufacturers Association.

Heat Exchanger (2016). Retrieved June 4, 2017 from https://en.wikipedia.org/wiki/Heat_exchanger.

Heberle, F., & Brüggemann, D. (2010). Exergy based fluid selection for a geothermal Organic Rankine Cycle for combined heat and power generation. *Applied Thermal Engineering*, *30*(11), 1326-1332.

Hepbasli, A., & Ozgener, L. (2004). Development of geothermal energy utilization in Turkey: a review. *Renewable and Sustainable Energy Reviews*, *8*(5), 433-460.

Hosseini, M. J., Rahimi, M., & Bahrampoury, R. (2014). Experimental and computational evolution of a shell and tube heat exchanger as a PCM thermal storage system. *International Communications in Heat and Mass Transfer*, *50*, 128-136.

Hsieh, J. C., Fu, B. R., Wang, T. W., Cheng, Y., Lee, Y. R., & Chang, J. C. (2017). Design and preliminary results of a 20-kW transcritical organic Rankine cycle with a screw expander for low-grade waste heat recovery. *Applied Thermal Engineering*, *110*, 1120-1127.

Hybrid Plant. (2015). Retrieved June 4, 2017, from http://www.thinkgeoenergy.com/video-enels-stillwater-hybrid-geothermal-solar-plant-in-nevada

Indiamart. (2017). Retrieved June 4, 2017, from https://dir.indiamart.com/impcat/finned-tube-heat-exchangers.html

Institute for Energy Resourcefulness. (2017). Retrieved June 4, 2017 from http://www.energyresourcefulness.org/Power/solar.html

Ishihara, K., Palen, J. W., & Taborek, J. (1980). Critical review of correlations for predicting two-phase flow pressure drop across tube banks. *Heat Transfer*

Engineering, *1*(3), 23-32.

Jayakumar, J. S., Mahajani, S. M., Mandal, J. C., Vijayan, P. K., & Bhoi, R. (2008). Experimental and CFD estimation of heat transfer in helically coiled heat exchangers. C*hemical Engineering Research and Design*, *86*(3), 221-232.

Kakac, S., Liu, H., & Pramuanjaroenkij, A. (2012). *Heat exchangers: selection, rating, and thermal design*. USA: CRC Press.

Kalogirou, S. A. (2004). Solar thermal collectors and applications. *Progress in Energy and Combustion Science*, *30*(3), 231-295.

Kalogirou, S. A. (2013). *Solar energy engineering: processes and systems*. USA: Elsevier Academic Press.

Kandlikar, S. G. (1990). A general correlation for saturated two-phase flow boiling heat transfer inside horizontal and vertical tubes. *ASME Journal Heat Transfer*, *112*(1), 219-228.

Kara, Y. A., & Güraras, Ö. (2004). A computer program for designing of shell-and-tube heat exchangers. *Applied Thermal Engineering*, *24*(13), 1797-1805.

Kerme, E. D., Orfi, J. (2015). Exergy-based thermodynamic analysis of solar driven organic Rankine cycle. *Journal of Thermal Engineering*, *1*(5), 192-202.

Kosmadakis, G., Landelle, A., Lazova, M., Manolakos, D., Kaya, A., Huisseune, H., & De Paepe, M. (2016). Experimental testing of a low-temperature organic Rankine cycle (ORC) engine coupled with concentrating PV/thermal collectors: Laboratory and field tests. *Energy*, *117*, 222-236.

Lazova, M., Huisseune, H., Kaya, A., Lecompte, S., Kosmadakis, G., & De Paepe, M. (2016). Performance evaluation of a helical coil heat exchanger working under

supercritical conditions in a solar organic Rankine cycle installation. *Energies*, *9*(6), 432.

Lei, Y. G., He, Y. L., Chu, P., & Li, R. (2008). Design and optimization of heat exchangers with helical baffles. *Chemical Engineering Science*, *63*(17), 4386-4395.

Linde Gas. (2015). Industrial Gases Retrived January 16, 2015, from http://www.linde-gas.com/en/index.html.

El Maakoul, A., Laknizi, A., Saadeddine, S., Abdellah, A. B., Meziane, M., & El Metoui, M. (2017). Numerical design and investigation of heat transfer enhancement and performance for an annulus with continuous helical baffles in a double-pipe heat exchanger. *Energy Conversion and Management*, *133*, 76-86.

Mago, P. J., Chamra, L. M., & Somayaji, C. (2007). Performance analysis of different working fluids for use in organic Rankine cycles. *Proceedings of the Institution of Mechanical Engineers, Part A: Journal of Power and Energy*, *221*(3), 255-263.

Marion, M., Voicu, I., & Tiffonnet, A. L. (2012). Study and optimization of a solar subcritical organic Rankine cycle. *Renewable Energy*, *48*, 100-109.

Nakaso, K., Mitani, H., & Fukai, J. (2015). Convection heat transfer in a shell-and-tube heat exchanger using sheet fins for effective utilization of energy. *International Journal of Heat and Mass Transfer*, *82*, 581-587.

National Renewable Energy Laboratory. (2010). : 4. http://www.nrel.gov/news/features/feature_detail.cfm/feature_id=1530 (June 4, 2017).

Taher, F. N., Movassag, S. Z., Razmi, K., & Azar, R. T. (2012). Baffle space impact

on the performance of helical baffle shell and tube heat exchangers. *Applied Thermal Engineering*, *44*, 143-149.

Ozden, E., & Tari, I. (2010). Shell side CFD analysis of a small shell-and-tube heat exchanger. *Energy Conversion and Management*, *51*(5), 1004-1014.

Patankar, S. (1980). *Numerical heat transfer and fluid flow*. USA: CRC Press.

Perry, R. H., & Green, D. W. (1999). *Perry's chemical engineers' handbook*. UK: McGraw-Hill Professional.

Qiu, G. (2012). Selection of working fluids for micro-CHP systems with ORC. *Renewable Energy*, *48*, 565-570.

Reppich, M., & Zagermann, S. (1995). A new design method for segmentally baffled heat exchangers. *Computers & Chemical Engineering*, *19*, 137-142.

Selbaş, R., Kızılkan, Ö., & Reppich, M. (2006). A new design approach for shell-and-tube heat exchangers using genetic algorithms from economic point of view. *Chemical Engineering and Processing: Process Intensification*, *45*(4), 268-275.

Shah, R. K., & Sekulic, D. P. (2003). *Fundamentals of heat exchanger design*. USA: John Wiley & Sons.

Shahril, S. M., Quadir, G. A., Amin, N. A. M., & Badruddin, I. A. (2017). Thermo hydraulic performance analysis of a shell-and-double concentric tube heat exchanger using CFD. *International Journal of Heat and Mass Transfer*, *105*, 781-798.

Shengjun, Z., Huaixin, W., & Tao, G. (2011). Performance comparison and parametric optimization of subcritical Organic Rankine Cycle (ORC) and transcritical power

cycle system for low-temperature geothermal power generation. *Applied Energy*, *88*(8), 2740-2754.

Singh, G., & Kumar, H. (2014). Computational Fluid Dynamics Analysis of Shell and Tube Heat Exchanger. *Journal of Civil Engineering and Environmental Technology*, *1*(3).

SkyTrough Fact Sheet. (2015). Retrieved May 14, 2016 from http://www.skyfuel.com/downloads/brochure/SkyTroughFactsheet.pdf

SkyTrough Next-Generation Solar Parabolic Trough Technology. (2009). Retrieved May 14, 2016 from http://www.skyfuel.com/downloads/brochure/SkyTroughBrochure.pdf.

Subramanian, R. S. (2004). Shell-and-Tube Heat Exchangers. Retrieved June 16, 2017 from http://web2.clarkson.edu/projects/subramanian/ch330/notes/Shell%20and%20Tube%20Heat%20Exchangers.pdf

Subramanian, R. S. How to Design a Shell-and-Tube Heat Exchanger (2010). Retrieved May 14, 2016 from http://web2.clarkson.edu/projects/subramanian/ch330/notes/Shell and Tube Heat Exchanger Design.pdf.

Tan, X. H., Zhu, D. S., Zhou, G. Y., & Yang, L. (2013). 3D numerical simulation on the shell side heat transfer and pressure drop performances of twisted oval tube heat exchanger. *International Journal of Heat and Mass Transfer*, *65*, 244-253.

Tempesti, D., & Fiaschi, D. (2013). Thermo-economic assessment of a micro CHP system fuelled by geothermal and solar energy. *Energy*, *58*, 45-51.

Union of Concerned Scientists. (2017). Retrieved June 4, 2017 from

http://www.ucsusa.org/clean-energy/renewable-energy#.WTLmFGiLS03

US' DOE Announces $20 M to integrate concentrated solar power with fossil fuel plants. (2012). Retrieved June 4, 2017 from http://csp-world.com/news/20121218/00670/us-doe-announces-20-m-integrate-concentrated-solar-power-fossil-fuels-plants.

Vetter, C., Wiemer, H. J., & Kuhn, D. (2013). Comparison of sub-and supercritical Organic Rankine Cycles for power generation from low-temperature/low-enthalpy geothermal wells, considering specific net power output and efficiency. *Applied Thermal Engineering*, *51*(1), 871-879.

Walraven, D., Laenen, B., & D'haeseleer, W. (2014). Comparison of shell-and-tube with plate heat exchangers for the use in low-temperature organic Rankine cycles. *Energy Conversion and Management*, *87*, 227-237.

Walraven, D., Laenen, B., & D'haeseleer, W. (2014). Optimum configuration of shell-and-tube heat exchangers for the use in low-temperature organic Rankine cycles. *Energy Conversion and Management*, *83*, 177-187.

Wang, E. H., Zhang, H. G., Fan, B. Y., Ouyang, M. G., Zhao, Y., & Mu, Q. H. (2011). Study of working fluid selection of organic Rankine cycle (ORC) for engine waste heat recovery. *Energy*, *36*(5), 3406-3418.

Wang, E., Yu, Z., Zhang, H., & Yang, F. (2017). A regenerative supercritical-subcritical dual-loop organic Rankine cycle system for energy recovery from the waste heat of internal combustion engines. *Applied Energy*, *190*, 574-590.

Wang, X., Zheng, N., Liu, P., Liu, Z., & Liu, W. (2017). Numerical investigation of shell side performance of a double shell side rod baffle heat exchanger. *International Journal of Heat and Mass Transfer*, *108*, 2029-2039.

Wang, Z. Q., Zhou, N. J., Guo, J., & Wang, X. Y. (2012). Fluid selection and parametric optimization of organic Rankine cycle using low temperature waste heat. *Energy*, *40*(1), 107-115.

Wind Hybrid Power Systems. (2016). Retrieved June 4, 2017, from https://en.wikipedia.org/wiki/Wind_hybrid_power_systems (June 4, 2017).

You, Y., Chen, Y., Xie, M., Luo, X., Jiao, L., & Huang, S. (2015). Numerical simulation and performance improvement for a small size shell-and-tube heat exchanger with trefoil-hole baffles. *Applied Thermal Engineering*, *89*, 220-228.

Zervos, A., (2016). Renewables 2016 global status report. Retrieved June 4, 2017, from http://www.ren21.net/status-of-renewables/global-status-report/.

Zhang, C., Liu, C., Wang, S., Xu, X., & Li, Q. (2017). Thermo-economic comparison of subcritical organic Rankine cycle based on different heat exchanger configurations. *Energy*, *123*, 728-741.

Zhang, J. F., He, Y. L., & Tao, W. Q. (2009a). 3D numerical simulation on shell-and-tube heat exchangers with middle-overlapped helical baffles and continuous baffles–Part I: Numerical model and results of whole heat exchanger with middle-overlapped helical baffles. *International Journal of Heat and Mass Transfer*, *52*(23), 5371-5380.

Zhang, J. F., He, Y. L., & Tao, W. Q. (2009b). 3D numerical simulation on shell-and-tube heat exchangers with middle-overlapped helical baffles and continuous baffles–Part II: Simulation results of periodic model and comparison between continuous and non continuous helical baffles. *International Journal of Heat and Mass Transfer*, *52*(23), 5381-5389.